

Summer 2012

# Gravity Anomalies Along the East Scotia Ridge: Constraining the Relative Importance of Magmatic and Tectonic Controls on Crustal Accretion

Briton Lee Nicholson

Follow this and additional works at: [https://digitalcommons.odu.edu/oeas\\_etds](https://digitalcommons.odu.edu/oeas_etds)



Part of the [Geology Commons](#), [Geophysics and Seismology Commons](#), and the [Tectonics and Structure Commons](#)

---

## Recommended Citation

Nicholson, Briton L.. "Gravity Anomalies Along the East Scotia Ridge: Constraining the Relative Importance of Magmatic and Tectonic Controls on Crustal Accretion" (2012). Master of Science (MS), Thesis, Ocean & Earth Sciences, Old Dominion University, DOI: 10.25777/hb4s-j551  
[https://digitalcommons.odu.edu/oeas\\_etds/368](https://digitalcommons.odu.edu/oeas_etds/368)

This Thesis is brought to you for free and open access by the Ocean & Earth Sciences at ODU Digital Commons. It has been accepted for inclusion in OES Theses and Dissertations by an authorized administrator of ODU Digital Commons. For more information, please contact [digitalcommons@odu.edu](mailto:digitalcommons@odu.edu).

**GRAVITY ANOMALIES ALONG THE EAST SCOTIA RIDGE:  
CONSTRAINING THE RELATIVE IMPORTANCE OF MAGMATIC AND TECTONIC  
CONTROLS ON CRUSTAL ACCRETION**

by

Briton Lee Nicholson  
B.S. December 2009, Old Dominion University

A Thesis Submitted to the Faculty of Old Dominion University in Partial Fulfillment  
of the Requirements for the Degree of

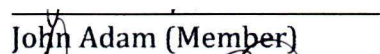
MASTER OF SCIENCE

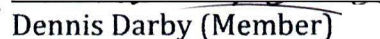
OCEAN AND EARTH SCIENCES

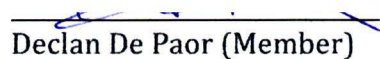
OLD DOMINION UNIVERSITY  
August 2012

Approved by:

  
Jennifer Georgan (Director)

  
John Adam (Member)

  
Dennis Darby (Member)

  
Declan De Paor (Member)

## **ABSTRACT**

### **GRAVITY ANOMALIES ALONG THE EAST SCOTIA RIDGE: CONSTRAINING THE RELATIVE IMPORTANCE OF MAGMATIC AND TECTONIC CONTROLS ON CRUSTAL ACCRETION**

Briton Lee Nicholson  
Old Dominion University, 2012  
Director: Dr. Jennifer Georgen

Similar to regions such as the Lau Basin and the Caribbean Sea, the eastern Scotia Sea is a geologically complex area that involves multiple plate boundary types. This study uses bathymetry and gravity data to infer upper mantle geodynamics in the eastern Scotia Sea region. Beneath this region is an intermediate-rate back-arc spreading center known as the East Scotia Ridge (ESR) that forms the boundary between the Scotia and Sandwich plates. To the east of the ESR are the South Sandwich island arc and the South Sandwich Trench. The ESR is a relatively young feature, with spreading estimated to have begun ~20 Ma (Livermore, 2003).

Earlier studies examining trends in bathymetry and geochemistry along the north-south striking ESR (e.g., Livermore, 2003) suggested that westward-directed flow from the Bouvet plume, located approximately 2000 km to the east, may affect ridge magmatic processes at segments near the slab ends, particularly in the north. In this investigation mantle Bouguer anomaly (MBA) is calculated for the eastern Scotia Sea to evaluate the relative importance of magmatic and tectonic factors in controlling crustal accretion along the ESR.

MBA values do not indicate the presence of enhanced, plume-dominated upwelling beneath the northernmost and southernmost segments. Likewise, geochemical data from published sources do not show a clear thermal plume influence. Overall, a mechanism of geochemical source heterogeneity plus enhanced melting due to plate boundary geometry, rather than a “classic” thermal plume, is preferred to explain geophysical anomalies along the ESR.

## **ACKNOWLEDGEMENTS**

I am very thankful to several professors at Old Dominion University for giving me the tools, without which the completion of my thesis would not have been possible. My advisor, Dr. Georgen, provided me a tremendous amount of guidance and patiently dedicated time to address all of my questions. Drs. Bochdansky, Georgen, and Klinck introduced me to Matlab and encouraged me to become proficient in data analysis. I am also thankful to each of my committee members for their valuable suggestions for the improvement of my thesis.

## TABLE OF CONTENTS

|   | Page |
|---|------|
| LIST OF FIGURES .....   | v    |
| INTRODUCTION AND OVERVIEW .....   | 1    |
| BACKGROUND INFORMATION .....  | 4    |
| Relative Plate Motion Between South America and<br>Antarctica .....   | 4    |
| The East Scotia Ridge .....   | 5    |
| Effect of the Bouvet Plume on Crustal Accretion in the<br>Southern Atlantic Ocean .....                       | 5    |
| Ridge Segmentation and the Influence of Spreading Rates .....   | 9    |
| METHODOLOGY .....   | 14   |
| Bathymetry and Free-Air Anomaly .....   | 14   |
| Mantle Bouguer Anomaly .....  | 19   |
| RESULTS .....   | 21   |
| Bathymetry .....  | 21   |
| Free-Air Anomaly .....  | 24   |
| Ridge Propagation .....   | 25   |
| Mantle Bouguer Anomaly .....  | 27   |
| Geochemistry .....  | 32   |
| Regressions .....   | 39   |
| DISCUSSION .....  | 43   |
| The Thermal Plume Mechanism as the Cause of Geophysical and<br>Geochemical Variations in the ESR Region ..... | 43   |
| Alternative Mechanism: Mantle Geochemical Heterogeneity .....   | 46   |
| CONCLUSIONS .....   | 52   |
| REFERENCES .....  | 53   |
| VITA .....  | 58   |

## LIST OF FIGURES

| Figure  | Page |
|---|------|
| 1. Geographic and bathymetric map of the Scotia Sea region .....  | 2    |
| 2. Schematic profile of a plume-affected MOR .....  | 6    |
| 3. Regions with Bouvet plume geochemical affinity .....   | 8    |
| 4. Model of along-axis MAR (i.e., slow spreading ridge) subseafloor<br>density .....  | 11   |
| 5. Plot of segment length vs. relief (or $\Delta$ bathy) for the MAR and<br>SWIR .....  | 12   |
| 6. FAA map of the ESR region .....  | 16   |
| 7. Bathymetry of the ESR region .....   | 18   |
| 8. Axial profiles of ESR (a) bathymetry, (b) spreading rate and<br>segment length, and (c) ESR-SST separation distance .....                            | 23   |
| 9. Profile of FAA along the ESR .....   | 26   |
| 10. MBA map of the ESR region .....   | 29   |
| 11. Profiles of (a) MBA, (b), $\Delta$ MBA, (c) $^{87}\text{Sr}/^{86}\text{Sr}$ and $\Delta$ bathy, and<br>$\text{Na}_8$ and $\text{Fe}_8$ values ..... | 31   |
| 12. Boxplots of $\text{Na}_8$ of for segments E1-E9 .....   | 34   |
| 13. Boxplots of $\text{Fe}_8$ for segments E1-E9 .....  | 36   |
| 14. Boxplots of $^{87}\text{Sr}/^{86}\text{Sr}$ for segments E1-E9 .....  | 38   |
| 15. Plots of segment length vs. $\Delta$ bathy for the SWIR (Cannat et al.,<br>1999), MAR (Cannat et al., 1999) and ESR .....                           | 40   |
| 16. Sample of six of a total of 24 regression plots.....  | 42   |
| 17. Schematic of a heterogeneous mantle beneath a MOR .....   | 48   |
| 18. Schematic of a geochemically heterogeneous mantle with plume .....  | 51   |

## INTRODUCTION AND OVERVIEW

The eastern Scotia Sea is located between the South American and Antarctic Plates, in the southern portion of the Atlantic Ocean (Fig. 1). In general, geological processes in the eastern Scotia Sea have been studied less than those for other ocean regions, such as the northern Atlantic Ocean or eastern Pacific Ocean, because of the relative remoteness of the southern Atlantic. However, bathymetry and gravity data derived from satellites, as well as a series of recent cruises to the Scotia Sea, allow the geodynamics of the area to be investigated more thoroughly than previously possible.

The Scotia Sea is a geologically active region. The East Scotia Ridge (ESR), located in the eastern portion of the Scotia Sea, is a back-arc spreading center that forms the boundary between the Scotia (SCO) and Sandwich (SAN) plates. To the east of the ESR is a subduction-related chain of islands called the South Sandwich island arc. Subduction occurs farther to the east at the South Sandwich Trench (SST), which delineates the eastern margin of the Sandwich Plate. Because it contains a variety of plate boundary types over a relatively small geographical area, the eastern Scotia Sea is well-suited for exploring upper mantle flow fields in a geologically complex area.

One aim of this study is to investigate how oceanic crustal accretion and magmatic processes along the ESR are affected by long-wavelength upper mantle geodynamic processes over the scale of the southern Atlantic Ocean. Bathymetric and geochemical anomalies along the ESR axis have been interpreted as indicating affinity with the Bouvet mantle plume (e.g., Leat et al., 2000; Pearce et al., 2001; Fretzdorff et al., 2002; Livermore, 2003), which is located at 54°24'S, 3°24'E. The relationship between the ESR and the Bouvet plume is an interesting geologic problem, because while geodynamical interactions between plumes and ridges usually occur over a distance of ~1500 km or less (Ribe, 1996; Ito et al., 2003), the ESR and Bouvet are

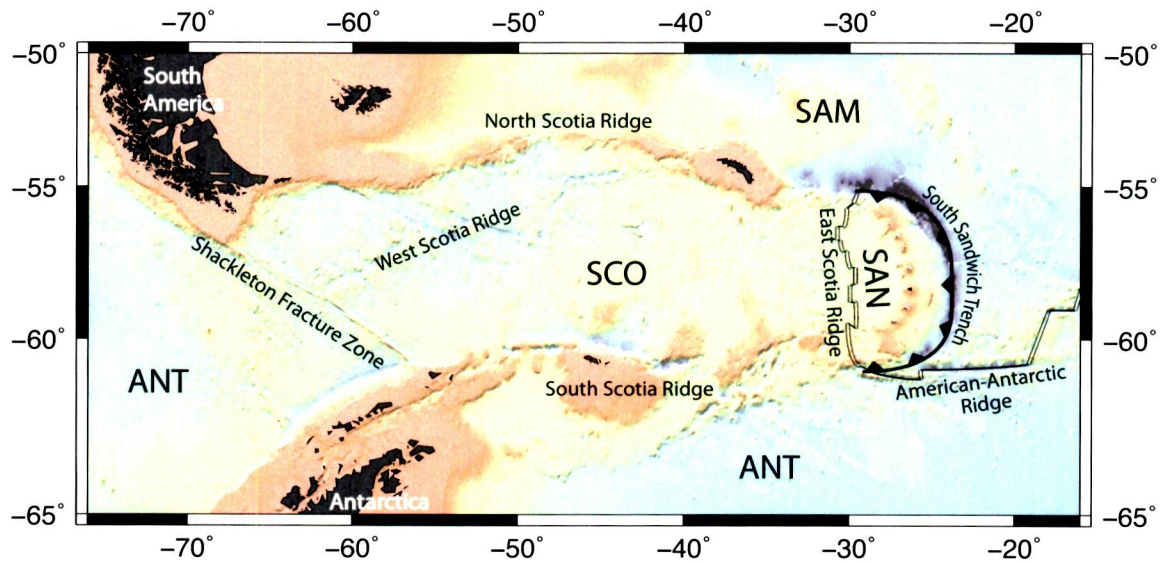


**Fig. 1.** Geographic and bathymetric map of the Scotia Sea region. Four tectonic plates are shown: South American (SAM), Sandwich (SAN), Scotia (SCO), and Antarctic (ANT). The toothed line indicates subduction at the South Sandwich Trench. Divergence occurs at the East Scotia Ridge and American-Antarctic Ridge. The North Scotia Ridge, South Scotia Ridge, and the Shackleton Fracture Zone are transform boundaries.



separated by approximately 2000 km. Another goal of this investigation is to examine how crustal accretion processes along the ESR vary at the scale of individual ridge segments. Previous studies have quantified systematic relationships between spreading rate, ridge segment length, gravity, and bathymetry for other global spreading centers such as the Mid-Atlantic Ridge (MAR) and Southwest Indian Ridge (SWIR) (e.g., Lin et al., 1990; Cannat et al., 1999). If a ridge such as the ESR follows these relationships, it suggests that plate boundary lithospheric or tectonic processes are important in the creation of oceanic crust. However, deviation from the relationships indicates that other factors may be involved, such as broad-scale thermal input from a mantle plume source causing excess magmatism.

The primary data used in this study are seafloor bathymetry and free-air gravity anomaly (FAA), which are used to calculate mantle Bouguer anomaly (MBA). MBA maps can be interpreted in terms of density heterogeneities in the crust and upper mantle, which can then be used to infer geodynamical processes. This investigation focuses on the region between longitudes 40°W and 20°W and latitudes 50°S and 65°S. This study area includes the ESR as well as the SST. Overall, variations in bathymetry and MBA are used to contrast the importance of magmatic and tectonic factors in controlling crustal accretion along the ESR.

## BACKGROUND INFORMATION

### Relative Plate Motion Between South America and Antarctica

Many of the tectonic features in the Scotia Sea region are a result of relative motion between southern South America (SSA) and the Antarctic Peninsula (AP). Approximately 150 Ma, the southern tip of SSA was adjacent to the northern tip of the AP (Cunningham et al., 1995). The two features separated by mid-Cretaceous time (~100 Ma), and westward motion of SSA began to outpace that of the AP by roughly 84 Ma (Cunningham et al., 1995).

Relative plate motions around the boundaries of the Scotia Sea region changed significantly over the past ~30 Myr. The Scotia Sea is presently bordered in the west by the Shackleton Fracture Zone, which is a left-lateral transform fault that separates SCO from the Antarctic Plate (ANT) (Fig. 1). A proto-Shackleton Fracture Zone accommodated most of the westward motion of SSA relative to AP until 30 Ma, at which time the Shackleton Fracture Zone became active (Cunningham et al., 1995). From about 30 Ma to 9 Ma, 700 km of east-west (strike-slip) and 440 km of north-south (divergent) motion occurred between SSA and AP due to plate motion along the now-inactive West Scotia Ridge and the Shackleton Fracture Zone (Cunningham et al., 1995). Around 30 Ma, the North Scotia Ridge became the northern boundary of newly generated seafloor in the west Scotia Sea (Cunningham et al., 1995). Since ~20 Ma, approximately 270 km of relative east-west SSA-AP motion has taken place along the North Scotia Ridge (Eagles, et al., 2005). The South Scotia Ridge, which previously formed as a magmatic arc, became a transform boundary about 20 Ma (Cunningham et al., 1995).

### The East Scotia Ridge

The ESR is a divergent plate boundary between SCO and SAN. Spreading along the ESR began approximately 21 Ma (Livermore, 2003), and the initiation of ESR divergence resulted in a decrease in spreading rate for the West Scotia Ridge. The half-spreading rate in the West Scotia Ridge was approximately 2.4-2.6 cm/yr from 26.5 Ma to 17 Ma, but it decreased to about 1-1.2 cm/yr from 17 Ma to 6 Ma (Lagabrielle et al., 2009). At approximately 17 Ma, the ESR replaced the West Scotia Ridge as the site of fastest spreading in the Scotia Sea (Livermore, 2003).

Divergence along the ESR is partially caused by SSA-AP relative motion; however, recent spreading rates in the ESR greatly exceed the relative motion between SSA and the AP (Eagles et al., 2005). The additional velocity component is due to trench rollback at the SST (Eagles et al., 2005). Present day divergence of the north-south striking ESR occurs in an east-west direction at intermediate rates. Full spreading rates are 6.0 cm/yr at the northern end, 7.0 cm/yr at ~58°S, and 6.8 cm/yr at the southern end (Thomas et al., 2003). Spreading at the ESR's southernmost segment began within the past 1 Myr (Livermore, 2003).

### Effect of the Bouvet Plume on Crustal Accretion in the Southern Atlantic Ocean

Trends in bathymetry and geochemistry along the ESR have been attributed in part to influence from the Bouvet mantle plume source (e.g., Leat et al., 2000; Pearce et al., 2001; Fretzdorff et al., 2002; Livermore, 2003). Mantle plumes affect approximately 20% of the length of the Earth's mid-ocean ridge (MOR) system (Ito et al., 2003). A mantle plume is defined by the upwelling of unusually hot, and therefore buoyant, material originating at a thermal boundary layer in the mantle or at the core-mantle boundary (Ito et al., 2003). Once a plume rises to the base of the lithosphere, material from the plume may be focused towards and along a MOR, along the "inverted duct" created by cooling and thickening lithospheric plates (Fig. 2). Examples of plume-ridge interactions include the Iceland/MAR, Galapagos/

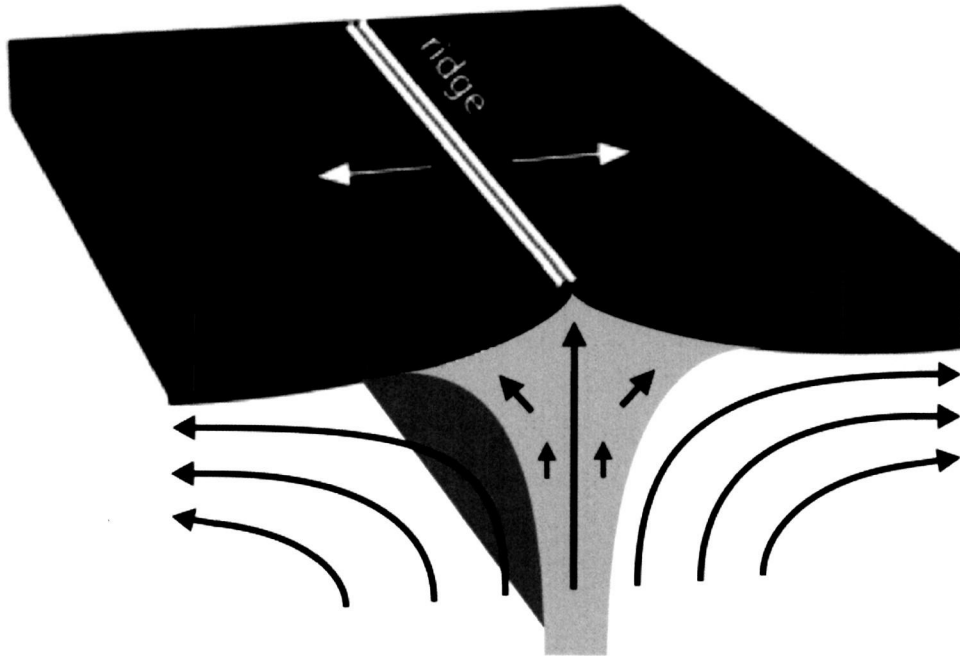


**Fig. 2.** Schematic profile of a plume-affected MOR. Lines and arrows in the mantle show the direction of upwelling beneath a ridge. Thermally buoyant plume material rises under a mid-ocean ridge axis and spreads along an “inverted duct” formed by the cooling and thickening lithospheric plates. Dark grey indicates spreading lithospheric plates and the grey regions beneath the ridge represent a plume.

Galapagos Spreading Center, and Azores/MAR systems (Ito and Lin, 1995; Ito et al., 1996; Moreira et al., 1999; Toomey et al., 2001; Canales et al., 2002; Moreira and All  gre, 2002; Ito et al., 2003 and references therein). Where plumes and ridges interact, the seafloor is generally marked by anomalies in depth and gravity, crustal thickness is often elevated, and mid-ocean ridge basalt (MORB) can have anomalous geochemistry. Numerical modeling results indicate that plumes and ridges generally only interact when separated by less than 1500 km (Ribe, 1996).

The Bouvet plume is a region of anomalous mantle located near the Bouvet triple junction, which is defined by the intersection of the SWIR, MAR, and American-Antarctic Ridge (AAR) (Fig. 3). Geochemically, samples with Bouvet plume affinity (e.g., high concentrations of incompatible elements, low Zr/Nb ratios, and high Zr/Y and La/Yb ratios) are dredged to at least 16  E along the SWIR axis, and perhaps as far as 25  E (le Roex et al., 1983; le Roex et al., 1992; Standish et al., 2008). Enriched MORB is also found along the AAR, but not as abundantly as along the SWIR (le Roex et al., 1985). Geophysically, however, the effects of the Bouvet plume appear to be more localized. Gravity data suggest that the influence of the Bouvet plume on the SWIR is generally limited to a length of the ridge between the Islas Orcadas and Bouvet FZs, a distance of only ~100-200 km (Georgen et al., 2001). The amplitudes of anomalies in gravity and bathymetry are also lower for the Bouvet/SWIR system than for other hotspot-affected ridges. For example, the low in MBA imparted to the SWIR by the plume is about -100 mGal (Georgen et al., 2001), compared to -300 mGal for the Iceland/MAR system (Ito and Lin, 1995). Overall, therefore, the apparent widespread distribution of the Bouvet geochemical signature contrasts with more localized anomalies in bathymetry and gravity.

In some subduction zones such the Tonga Trench, asthenospheric flow driven by slab retreat may enter the back-arc basin by advecting around slab ends or through gaps in the torn subducting plate (Keller et al., 2008). Similarly, it has been suggested that westward-flowing mantle with Bouvet plume characteristics enters the back-arc region of the SST (Fig. 3) (e.g., Livermore, 2003). Under this hypothesis,

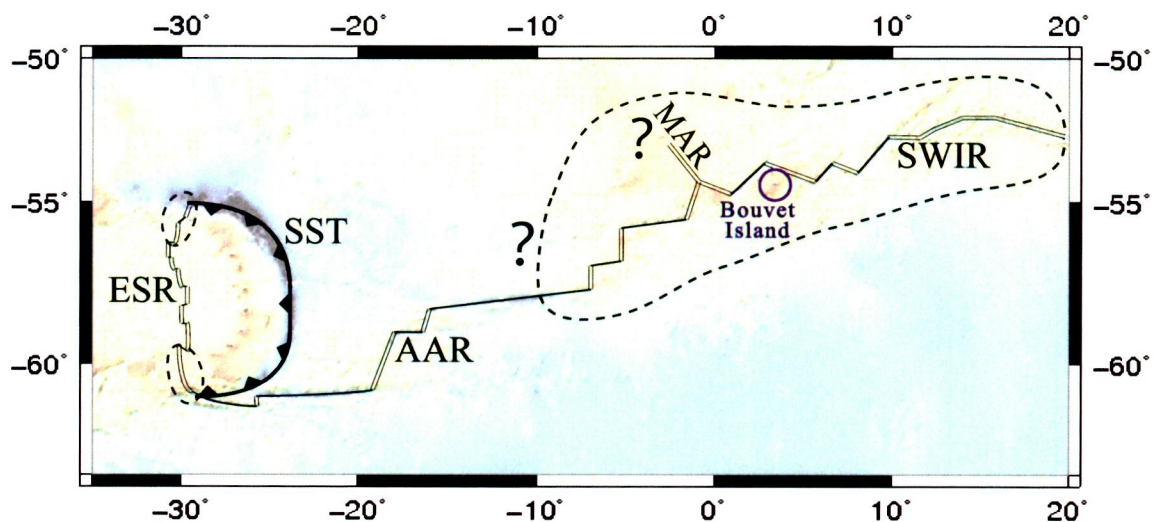


**Fig. 3.** Regions with Bouvet plume geochemical affinity. Dashed lines enclose the potentially affected areas (le Roex et al., 1983; le Roex et al., 1992; Leat et al., 2000; Fretzdorff et al., 2002; Georgen et al., 2003). The background map shows relative variations of seafloor depth, with lighter yellow colors indicating shallower bathymetry.

asthenospheric flow enters the melting region of the ESR via slab tears in the north and along the AAR in the south. Such flow could help to explain observed anomalies in seafloor depth and basalt geochemistry along the northernmost and southernmost ESR segments (Leat et al., 2000; Pearce et al., 2001; Fretzdorff et al., 2002; and Livermore, 2003). However, direct interaction of the Bouvet plume with the ESR would not be expected based on the small seafloor expression of the Bouvet plume, with the localized geophysical effects described previously (Georgen et al., 2001), and the ~2000 km distance between the plume and the Scotia Sea. Thus, the mechanism by which an apparent Bouvet plume signature is found along the northern and southern ESR is an unresolved question.

### Ridge Segmentation and the Influence of Spreading Rates

Geological activity at a MOR is largely a balance of two types of processes. Tectonic processes are related to lithospheric faulting and plate boundary segmentation, while magmatic processes refer to the upwelling and thermal regime underlying the lithosphere. Segmentation is a fundamental characteristic of Earth's MOR system, with discontinuities occurring every 10 to 1000 km along spreading centers (Macdonald et al., 1988). Offsets between segments may be in the form of transform faults, which are often 50 km long or more, or in the form of discontinuities called overlapping spreading centers (OSCs), in which the ends of adjacent segments overlap along the ridge axis. In OSCs, the offset in the direction of spreading is typically only 0.5 to 10 km, and the length of overlap along axis is typically three times the distance of the offset (Macdonald et al., 1988).

The ESR has ten segments, numbered E1 to E10 from north to south. E10 is not considered in this study because it is located entirely within the subduction zone, where compressive stress is likely the dominant force, rather than tectonic extension. The SST also influences segments E1 and E9. The depth of E1 is much greater than adjacent segment E2 due to the trench, and segment E9 curves sharply to the east at its southern end as it nears the SST. Overall, the ESR segments are relatively short, with

mean and median length of about 50 km. The shortest segments are E1, E4, and E5, with lengths of approximately 20 km, 30 km, and 40 km, respectively. The longest segments are E8, E9, and E2, with lengths of about 90 km, 80 km, and 60 km, respectively.

In general, ESR segment discontinuities are characterized by small lateral offsets, with half of the discontinuities taking the form of OSCs. For this study, the offset between segments is defined as the longitudinal distance between the southernmost point of one segment and the northernmost point of the segment to the south of it. Mean and median offsets are roughly 30 km and 23 km, respectively. Greater offsets (~50-60 km) occur near the northern and southern ends of the ridge, while the smallest offsets (~10-20 km) occur near the center of the ridge.

The overlap between segments is defined as the distance, measured in latitude and converted to kilometers, shared by two adjacent ridge segments. Considering only the four cases where ESR segments overlap, mean and median overlaps between segments are 7 km and 5 km, respectively. The greatest overlap, ~18 km, occurs between segments E8 and E9. Segments E4 and E5 overlap by approximately 1 km.

In MORs dominated by tectonic processes, segments generally have thicker crust at the segment center than at segment ends, and longer segments have greater intra-segment bathymetric relief than shorter ones (Fig. 4). Thus, plots of segment length vs. bathymetric relief show a positive, linear correlation (Fig. 5) (Lin et al., 1990; Cannat et al., 1999). Slopes are generally lower for plots of fast-spreading ridges, which reflects a smaller change in bathymetry between segment ends and segment centers. Slopes for slow-spreading ridges are steeper, due to greater bathymetric relief from segment center to segment end. The different slopes for fast and slow spreading ridges may be related to the style of underlying mantle upwelling (Lin and Phipps Morgan, 1992). Fast-spreading ridges are characterized by along-axis mantle upwelling that has a two-dimensional, sheet-like, or planar structure, whereas the along-axis mantle upwelling beneath slow-spreading ridges (Fig. 4) is



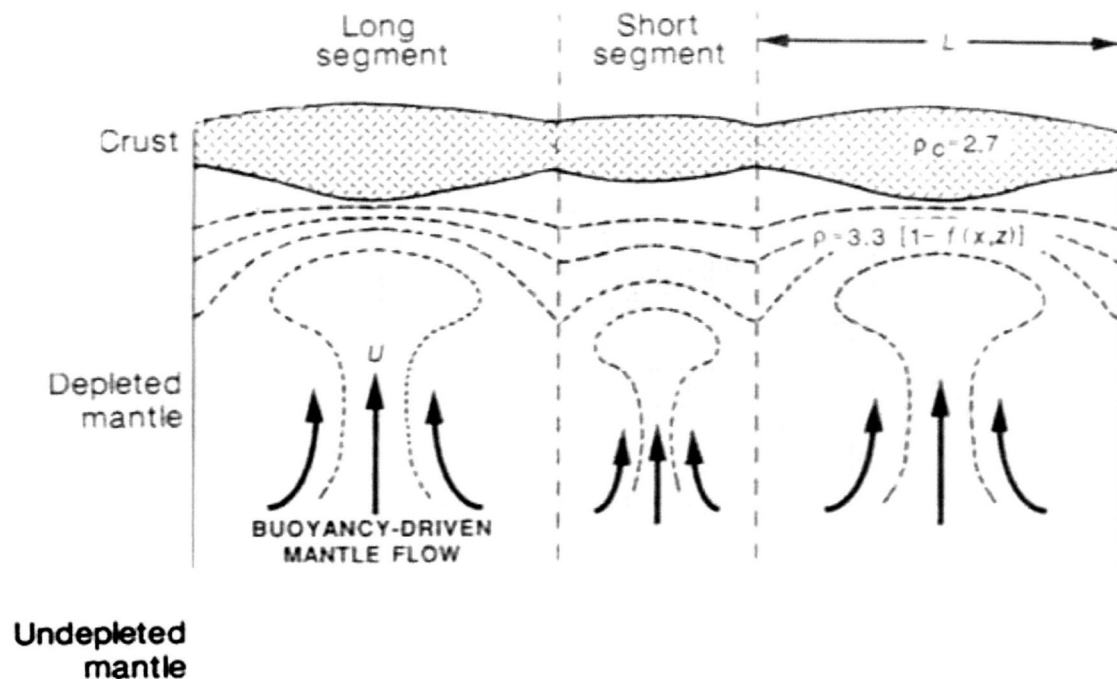


**Fig. 4.** Model of along-axis MAR (i.e., slow-spreading ridge) subseafloor density structure. In this model, mantle density is  $\rho = 3.3 \cdot [1 - f(x, z)] \cdot 10^6 \text{ g m}^{-3}$ , where  $f(x, z)$  depends on mantle temperature, amount of melt extraction, and amount of trapped basaltic melts. Crustal density,  $\rho_c$ , is  $2.7 \cdot 10^6 \text{ g m}^{-3}$ . The velocity of upwelling is denoted by  $U$ . Longer segments have thicker crust, greater bathymetric relief, and more focused upwelling. In general, intra-segment relief is greater in slow-spreading ridges and smaller in fast-spreading ridges. Figure from Lin et al. (1990).

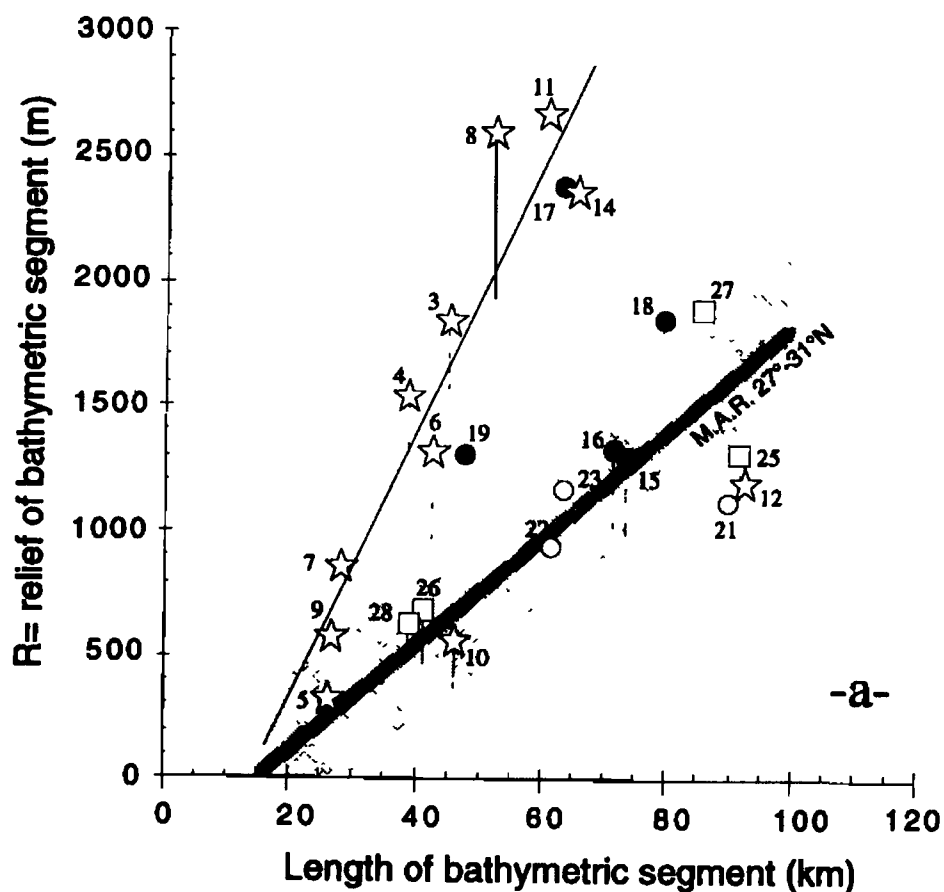


**Fig. 5.** Plot of segment length vs. relief (or  $\Delta$ bathy) for the MAR and SWIR. The thin black line is a regression line for SWIR segments from Cannat et al. (1999). The thick grey line is a regression line for MAR segments from Lin et al. (1990). Figure from Cannat et al. (1999).

generally more three-dimensional or diapiric (although the diapirs are significantly smaller in scale than those of mantle plumes) (Lin et al., 1990; Lin and Morgan, 1992). Thus, along-segment variations in crustal production are smaller for faster spreading ridges than for slower spreading ridges.

If a plot of segment length vs. bathymetric relief does not show a positive, linear correlation, it could indicate that a ridge is influenced by factors other than tectonic faulting and lithospheric processes. A ridge segment that experiences excess magmatism related to a plume, for example, may show less intra-segment bathymetric relief as the thermally cooler ridge discontinuities are warmed by hot upwelling mantle. Thus, plots of segment length vs. bathymetric relief for the ESR are useful in deconvolving magmatic and tectonic influences on crustal accretion.

## METHODOLOGY

### Bathymetry and Free-Air Anomaly

For this investigation, FAA data were obtained from a global gravity grid derived from satellite radar altimetry measurements (Sandwell and Smith, 1997; 2009) (Fig. 6). Bathymetry data were extracted from a global database that merges shiptrack depth measurements with seafloor topography calculated from satellite data (Smith and Sandwell, 1997) (Fig. 7). The resolution of both grids is 1-minute by 1-minute, which is appropriate for studying MOR segment-scale features. However, resolution constraints preclude the study of features with wavelengths less than ~20-30 km, such as detailed seafloor faulting patterns.

In marine applications, gravity measurements are either obtained using a shipboard marine gravimeter or calculated from satellite altimetric data. The International Gravity Formula is subtracted from gravity measurements to account for the rotation and oblate shape of the Earth (Blakely, 1996). When marine gravimeters are used, another correction, the Eotvos correction, is made to account for accelerations of the ship (Blakely, 1996). The resulting quantity, FAA, is the summation of the gravitational signals of all density contrasts below the sea surface, such as the interfaces between water and sediment, sediment and crust, and crust and mantle. Because FAA is proportional to the inverse of the square of the distance separating the sea surface and an interface between materials of contrasting density, marine FAA will be dominated by the interface between the water and the sediment covering the crust. Thus, FAA maps look very similar to bathymetry maps.

**Fig. 6.** FAA map of the ESR region. ESR segments are marked with solid black lines. White masking hides regions that are not well constrained by shiptrack bathymetry data. FAA data are taken from Sandwell and Smith (1997).

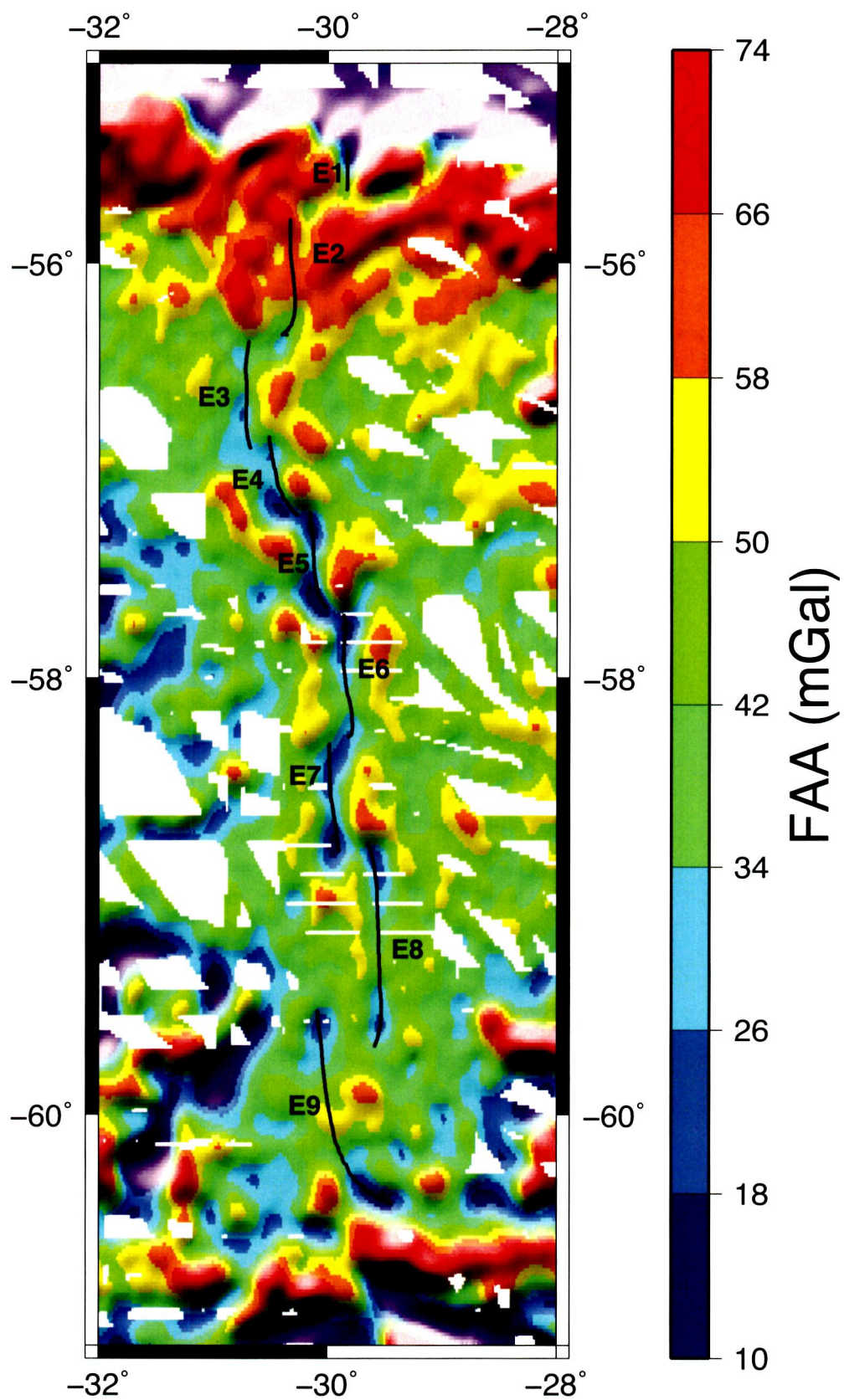
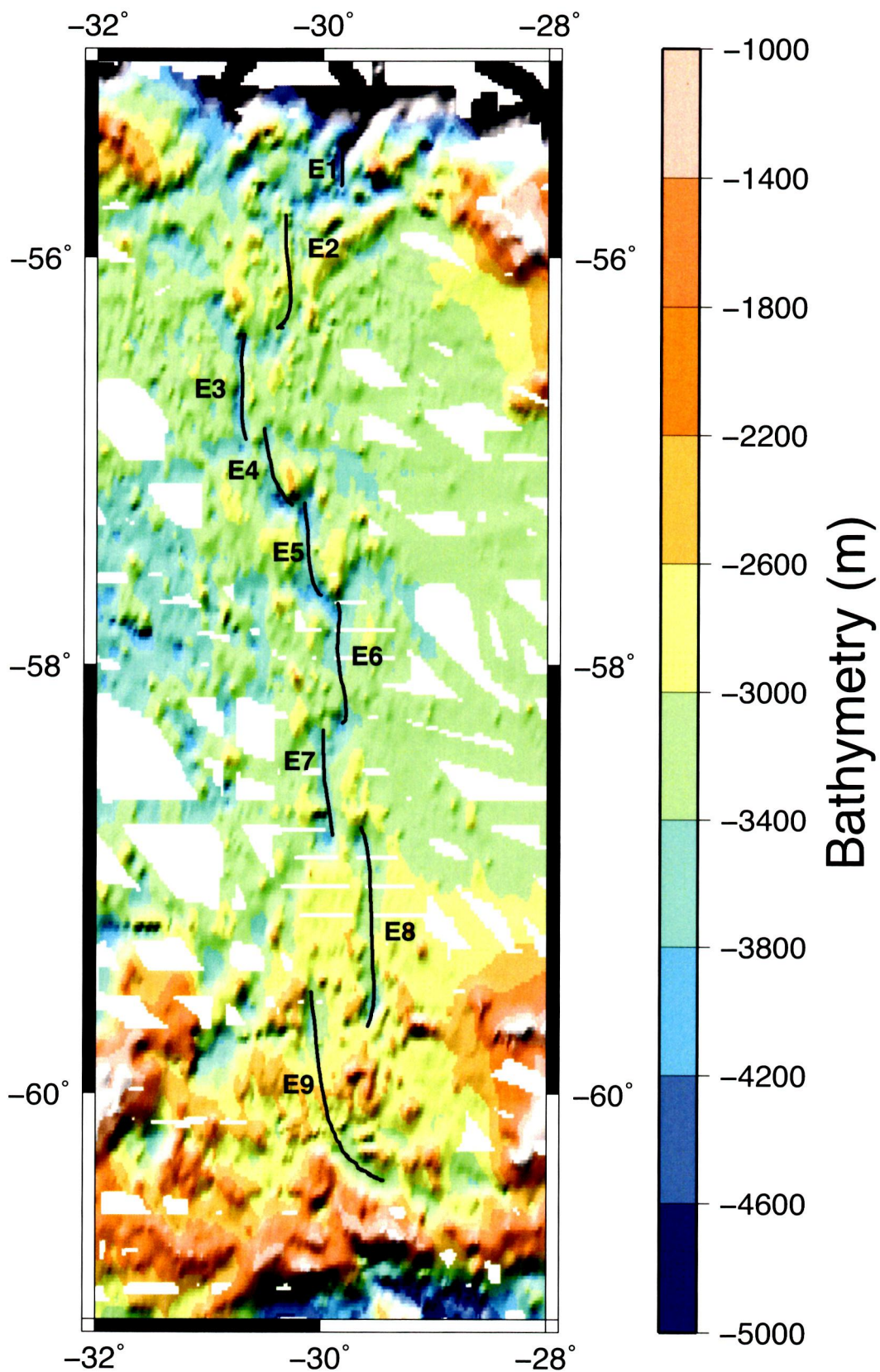


**Fig. 7.** Bathymetry of the ESR region. ESR segments E1 to E9 are marked with black lines and labeled. Most segments show well-defined axial troughs. White masking hides regions that are not well constrained by shiptrack bathymetry data. Seafloor depth data are from Sandwell and Smith (1997).





### Mantle Bouguer Anomaly

Because FAA is dominated by seafloor topography, it cannot be easily used to study the physical properties and inferred geodynamics of the underlying mantle. For this reason, mantle Bouguer anomaly (MBA) is calculated (Parker, 1973; Kuo and Forsyth, 1988; Lin et al., 1990). MBA can be used to infer crustal and mantle density variations, as well as variations in crustal thickness. Determination of MBA involves both bathymetry and FAA data. To ensure the independence of the gravity and bathymetry data sets during the calculation of MBA, only seafloor depths along shiptracks were used. Bathymetry data are better constrained in areas with greater shiptrack coverage. The best shiptrack coverage in the Scotia Sea is in the vicinity of the ESR (Fig. 7). Recurrent passes in the east-west direction cover about 1 degree of longitude on either side of ESR segments. Shiptrack coverage is also fairly dense in the area of the SST, South Sandwich island arc, and the North Scotia Ridge.

The MBA correction term represents the predicted gravity from a model that assumes that crustal and sediment layers have constant thickness and density, and that the water-sediment, sediment-crust, and crust-mantle interfaces all mimic seafloor topography. The correction term is calculated using distances from the sea surface to each interface, as well as assumed density contrasts across each interface. The thickness of the sediment and crustal layers were assumed to be 200 m and 6 km, respectively. The assumed crustal thickness is consistent with the global average oceanic crustal thickness of 5-7 km for non-hotspot-affected seafloor (e.g., Lin et al., 1990). The assumed sediment thickness is similar to the median sediment thickness of 193 m and the mean value of 219 m for the ESR region (Divins, 2003). Density contrasts across interfaces were calculated by subtracting the density of each layer from that of the one below it. The densities of the seawater, sediment, oceanic crust, and mantle were assumed to be 1.03 g/cm<sup>3</sup>, 2.3 g/cm<sup>3</sup>, 2.8 g/cm<sup>3</sup>, and 3.3 g/cm<sup>3</sup>, respectively. MBA was then determined by subtracting the MBA correction term from FAA data. Subtracting the correction term eliminates the gravitational

effects of seafloor topography and emphasizes smaller-amplitude, deeper density anomalies.

Maps of MBA consist of highs and lows in gravity, which can be interpreted to infer upper mantle processes (Lin et al., 1990; Lin and Morgan, 1992; Ito and Lin, 1995; Georgen et al., 2001; Ito et al., 2003; Georgen et al., 2003; Georgen, 2008; Georgen and Sankar, 2010). Relative MBA highs may result from higher density oceanic crust, higher density mantle, and/or thinner oceanic crust than was assumed during model calculations, or from older lithosphere, which is cooler and therefore more dense. Relative MBA lows may result from lower density oceanic crust or mantle, thicker oceanic crust, or young, hot lithosphere. Mantle plumes, which contain mantle material that is hotter and therefore less dense, and also tend to produce excess crust, are generally associated with MBA lows.

## RESULTS

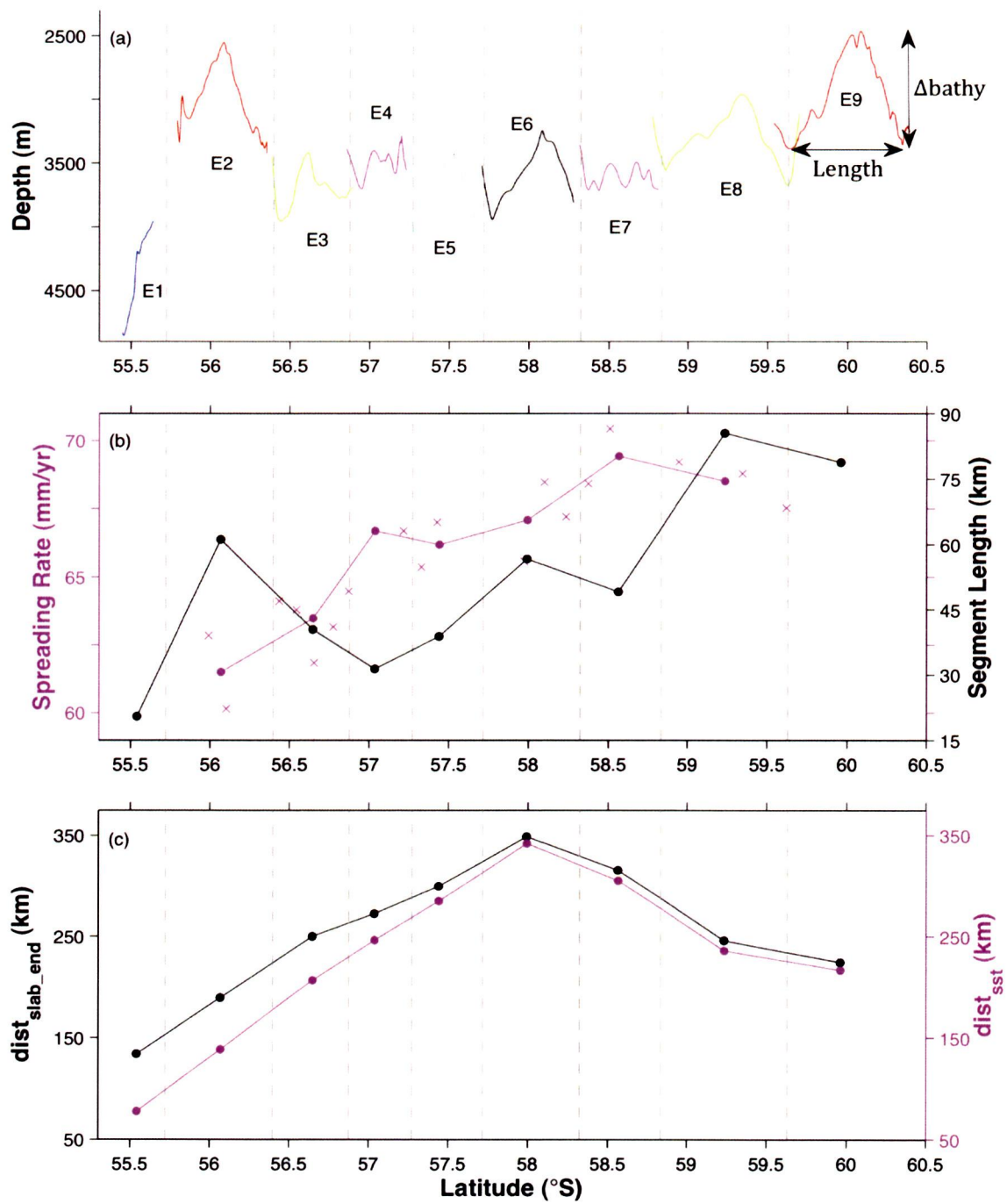
Seafloor depth and gravity show significant variations in the region around the ESR. In this section the results of MBA calculations are described and geophysical data are analyzed in several ways. Also, geochemical data such as  $^{87}\text{Sr}/^{86}\text{Sr}$ ,  $\text{Fe}_8$ , and  $\text{Na}_8$  are compiled from previously published sources for comparison against geophysical variables. Finally, regressions between four independent variables and six dependent variables are statistically analyzed to assess the major controls on the geodynamics of the ESR region. The independent variables are segment length, spreading rate, distance between each ESR segment and the nearest point on the SST, and distance between each ESR segment and the nearest subducting slab end, each of which characterizes plate kinematics in the Scotia Sea region. The dependent variables include bathymetry, gravity, and geochemistry data.

### Bathymetry

Seafloor depths in the ESR region are approximately 3.0 km for most of the area immediately surrounding the central part of the ridge (Fig. 7). Shallow areas ranging from 2.5 km to 3.0 km in depth surround segments E8 and E9. The deepest seafloor in the portion of the ESR region under investigation occurs in the north at the SST, where segment E1 intersects the periphery of the trench, and depths exceed 4.9 km.

Axial depths along the ESR range from about 2.5 km to 4.9 km (Fig. 8a). Mean and median axial depths for the entirety of the ridge are both approximately 3.4 km. For comparison, average global mid-ocean ridge depth is approximately 2.5 km (Parsons and Sclater, 1977). Neglecting E1, which is embedded within the domain of the trench, ESR segments at the northernmost and southernmost ends of the ridge are relatively shallower than those near the center. The shallowest points of the ESR occur at the centers of segments E2 and E9, with minimum depths of 2.6 km and 2.5 km, respectively. Segments E3-E7 range in depth from about 3.0 to 4.0 km. The deepest point along the ridge axis occurs in E5, which has a segment center depth of

**Fig. 8.** Axial profiles of ESR (a) bathymetry, (b) spreading rate and segment length, and (c) ESR-SST separation distance. Dashed grey lines through all subplots mark the boundaries between segments, which are labeled on panel (a). In (a), the method of determining segment length and bathymetric relief is shown for segment E9. In (b), individual values of spreading rate are marked with magenta "x"s (Thomas et al., 2003) and segment averages are shown by magenta dots, which are connected by a solid magenta line. Segment lengths are marked by black dots, which are connected by a solid black line. In (c), distances from ESR segment centers to the nearest slab end ( $\text{dist}_{\text{slab\_end}}$ ) are marked with black dots, which are connected by a solid black line. Distances from ESR segment centers to the nearest point on the SST ( $\text{dist}_{\text{sst}}$ ) are marked with magenta dots, which are connected by a solid magenta line.



3.5 km.

Where not affected by mantle plumes, intermediate-rate spreading centers such as the ESR typically have axial morphologies that range from shallow axial highs to subdued axial valleys (Carbotte and Macdonald, 1994). For the ESR, axial valleys are visible for at least part of the length of all ridge segments (Fig. 7). At the resolution of the bathymetry data, only the northern half of E2 and the center of E9 show distinct axial high structures.

As discussed in Chapter 1, for MOR segments in general, depths are shallower in the center and deeper at the ends. Following previous studies (e.g., Cannat et al., 1999; Lin et al., 1990), this study defines intra-segment change in bathymetry ( $\Delta$ bathy) as the vertical height difference between the shallowest point along a given segment (usually near the segment center) and the average of the deepest point on either side (usually near the segment ends) (Fig. 8a). Along the ESR, mean and median  $\Delta$ bathy are both approximately 0.7 km (Fig. 8c). An along-axis profile of  $\Delta$ bathy values forms a “w” shape, with the highest value of about 0.9 km at both segments E1 and E9. The lowest  $\Delta$ bathy occurs at segments E4 and E7, both of which have values of about 0.4 km.

### Free-Air Anomaly

A map of FAA near the ESR is very similar to that of bathymetry (Fig. 6), which is not surprising given the relationship between bathymetry and FAA discussed in Chapter 2 (Methodology). However, unlike bathymetry, the FAA map shows a generally decreasing trend along segments E2 to E9, from about 60-70 mGal in the north to about 30-40 mGal in the south. The lowest values of FAA (<10 mGal) occur to the north of segment E1, consistent with the proximity of this segment to the SST. FAA reaches values almost as low around 61°S, near the southern end of the trench. Axial valleys are visible in the gravity data. FAA generally decreases with distance away

from the ridge, with values of about 25-40 mGal in most areas at distances of 10-60 km from the axis. However, localized areas with high FAA, in the range of 40-60 mGal, also occur on the ridge flanks.

The along-axis FAA profile is generally similar to the profile for bathymetry (Fig. 9). One prominent feature is that the FAA at segment E1 changes significantly along its length, from about 11 mGal in the north to 47 mGal in the south, probably reflecting influence of the subduction zone. Over the entirety of the axial profile, highs in FAA occur at segments E2 (73 mGal) and E9 (57 mGal), while a low in FAA occurs at E6 (14 mGal). Each segment has a local FAA high in the center and lower values at the ends, except for E1. Notably, segment E7 shows a local high in the center, which is another difference between the FAA and bathymetry profiles. Because FAA is similar to bathymetry, and is subsumed by the calculation of MBA, it is not considered in additional detail for this study.

### Ridge Propagation

Ridge propagation occurs when one segment increases in length by overtaking an adjacent segment. Propagation is indicated by off-axis, v-shaped lineations in bathymetry and FAA, which point in the direction of propagation (e.g., Briaies and Rabinowicz, 2001). Ridge propagation can occur due to excess magmatism at a given segment, which then elongates at the expense of a neighboring, shortening segment (Briaies and Rabinowicz, 2001). Alternatively, ridge propagation may occur due to the rheological process of crack-tip formation and expansion (Phipps Morgan and Parmentier, 1995). Livermore (2003) found v-shaped ridges at the southern ends of segments E2 and E4, and the northern ends of segments E8 and E9, suggesting that E2 and E4 are propagating southward and E8 and E9 are propagating northward. In addition to these propagators, Schreider et al. (2011) add the southern portion of E1. The bathymetry and FAA maps used in this study indicate that only segments E2, E4, and E5 are propagating southward, while E9 is propagating to the north.

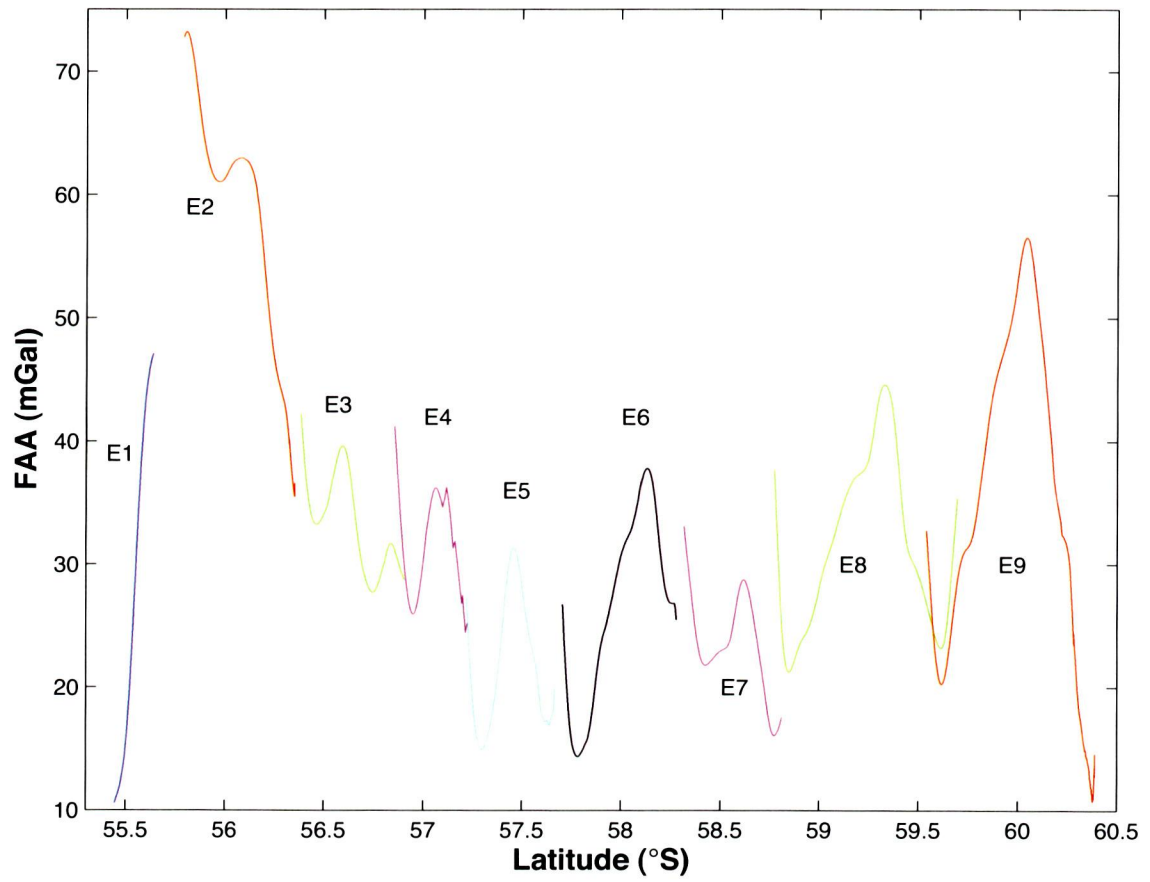


**Fig. 9.** Profile of FAA along the ESR. Lines denote FAA for individual ridge segments, which are labeled E1-E9.



### Mantle Bouguer Anomaly

For the ESR region under consideration, MBA varies more along-axis than laterally away from the ridge (Fig. 10). Near segments E1 to E3, MBA varies from about 30 mGal to 80 mGal. MBA generally decreases southward to segments E6 and E7, where it ranges from about -70 mGal to -120 mGal to the west of the axis, and from about -20 mGal to -90 mGal to the east. Farther to the south, MBA increases to values as high as 30 mGal near segment E8, and falls again to as low as -80 mGal near the southern portion of segment E9.

To find the degree to which segment-centered upwelling or other magmatic processes control the density structure along the ESR, intra-segment change in MBA ( $\Delta$ MBA) was calculated (Fig. 11). This parameter was calculated in the same way as  $\Delta$ bathy. Mean and median values of  $\Delta$ MBA for all ESR segments are about 50 mGal. The lowest  $\Delta$ MBA is at segment E2, with a value of about 20 mGal.  $\Delta$ MBA is relatively constant from E3 to E9, with a high of  $\sim$ 60 mGal at segment E4.

This method of calculating  $\Delta$ MBA, however, fails to highlight fully the dynamics of each segment, because it is influenced by the regional MBA variation. The general trend of decreasing MBA from north to south along the ESR noted for the MBA map is also apparent in axial profile. This trend is probably due to the higher-density SAM plate subducting beneath SAN. Thus, a long-wavelength planar trend was removed from the MBA map to highlight shorter-wavelength MBA variations. The equation of the removed trend was  $3.847x + 50.04y + 3.085z + 2,971 = 0$ . The resulting de-trended MBA is relatively high in the vicinity of segments E2 and E3, as well as segments E8 and E9 (Fig. 11a).

**Fig. 10.** MBA map of the ESR region. ESR segments are marked with solid black lines. White masking hides regions that are not well-constrained by shiptrack bathymetry data.

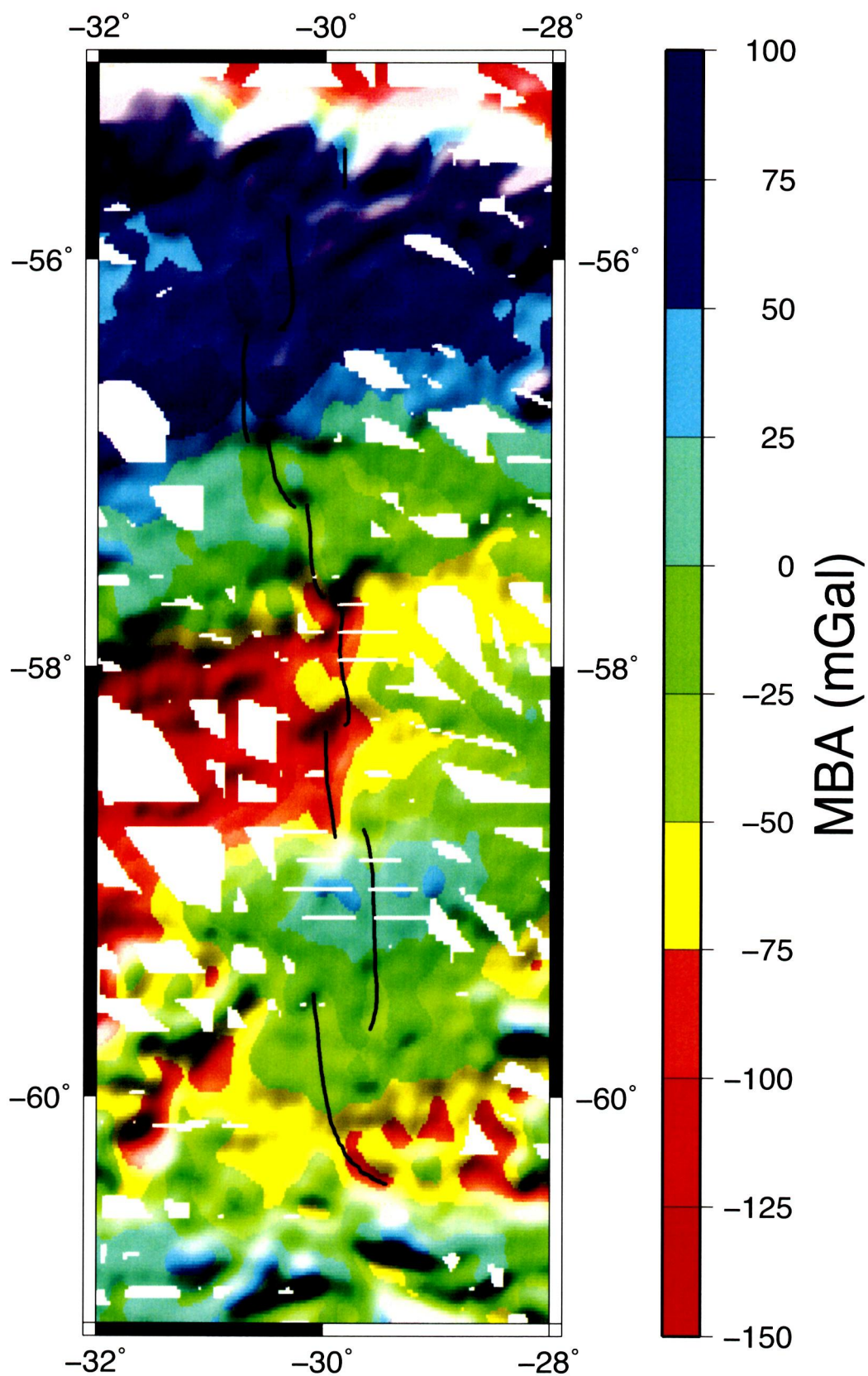
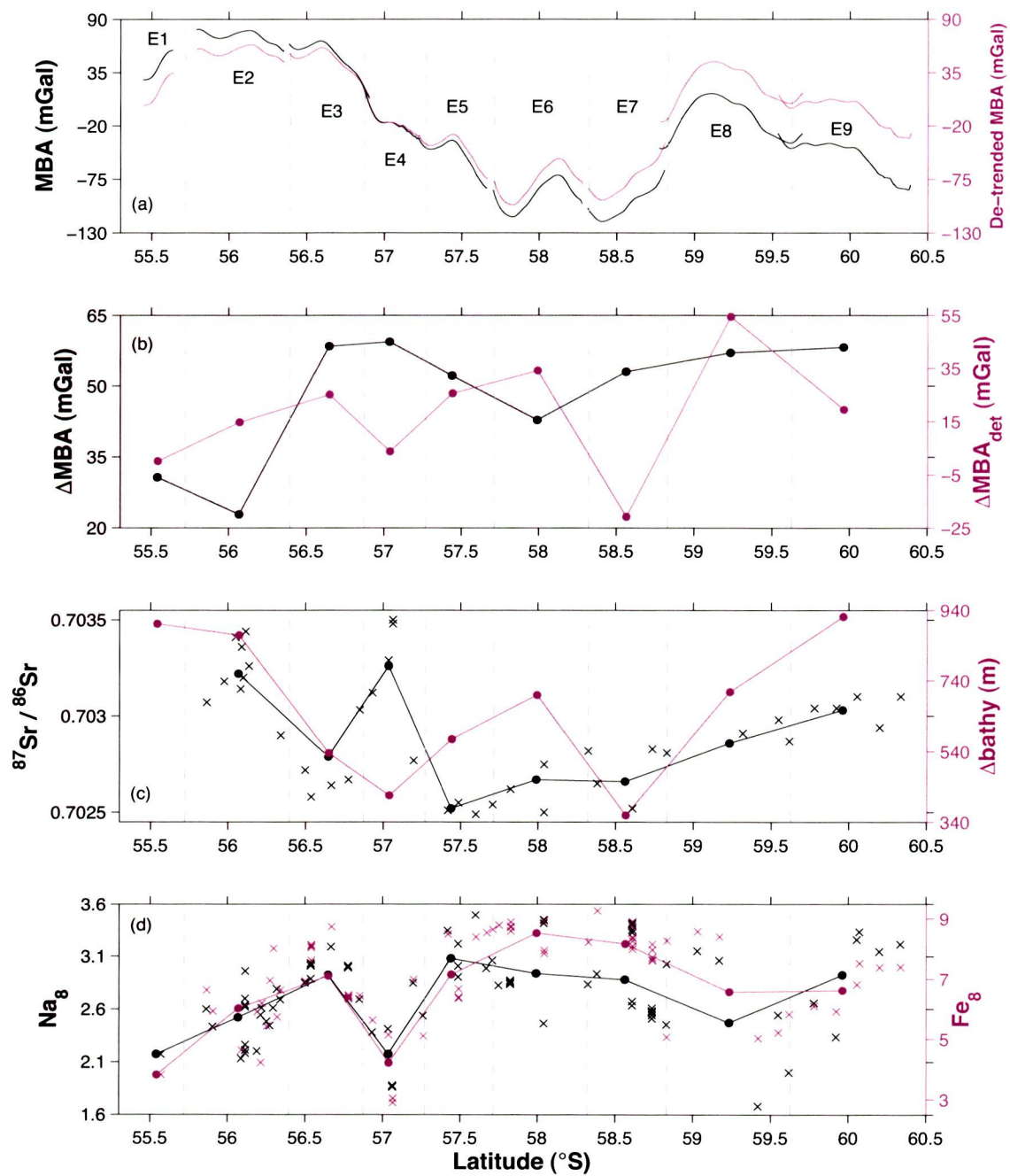


**Fig. 11.** Profiles of (a) MBA, (b)  $\Delta$ MBA, (c)  $^{87}\text{Sr}/^{86}\text{Sr}$  and  $\Delta$ bathy, and (d)  $\text{Na}_8$  and  $\text{Fe}_8$ . Dashed grey lines through all subplots mark the boundaries between segments. ESR segments are labeled on the MBA profile in panel (a). In panel (a), black lines denote a raw MBA data profile, and a de-trended MBA profile is shown with magenta lines. In panel (b), raw  $\Delta$ MBA values per segment are shown by black dots, which are connected by a black line. Values of the segment-scale de-trended change in MBA ( $\Delta\text{MBA}_{\text{det}}$ ) for each segment are denoted by magenta dots, which are connected by a solid magenta line. In panel (c),  $^{87}\text{Sr}/^{86}\text{Sr}$  values are denoted by black "x"s and segment averages are marked by black dots, which are connected by a solid black line. Magenta dots indicate  $\Delta$ bathy for each segment. In panel (d),  $\text{Na}_8$  values are marked by black "x"s and segment averages are shown by black dots, which are connected by a solid black line.  $\text{Fe}_8$  values are marked by magenta "x"s and segment averages are denoted by magenta dots, which are connected by a solid magenta line.



Similarly, to reduce the effect of the long-wavelength MBA trend on calculations of intra-segment change in MBA, another method of determining  $\Delta\text{MBA}$  was implemented (Fig. 11b). To calculate segment-scale de-trended MBA ( $\Delta\text{MBA}_{\text{det}}$ ), three values of de-trended MBA and their corresponding latitudes were identified for each ridge segment. First, a local de-trended MBA maximum was found near a segment center. Then, lows in de-trended MBA were found both to the north and to the south of the local maximum for the segment, and a line was fitted between the two lows on a profile of de-trended MBA vs. latitude. Finally, the difference was calculated between the high in de-trended MBA, and the value of the fitted line at the same latitude as the de-trended MBA high.  $\Delta\text{MBA}_{\text{det}}$  was determined in this way for all segments except E7, which has a low in de-trended MBA near the segment center. The calculation for E7 was done in the opposite way, with two de-trended MBA highs and one low.

Removing the long-wavelength trend in MBA and calculating  $\Delta\text{MBA}_{\text{det}}$  resulted in a parameter that emphasized magmatic process beneath ESR segments. Mean and median values of  $\Delta\text{MBA}_{\text{det}}$  for the ESR are both approximately 20 mGal.  $\Delta\text{MBA}_{\text{det}}$  increases almost linearly from segments E1 to E6, starting at about 0 mGal and reaching a peak of 34 mGal, although a value of about 4 mGal at E4 is lower than the linear trend.  $\Delta\text{MBA}_{\text{det}}$  is approximately -21, 54, and 19 mGal at segments E7, E8, and E9, respectively.

## Geochemistry

### *Degree and pressure of melting: $\text{Na}_8$ and $\text{Fe}_8$*

$\text{Na}_8$  is the concentration of  $\text{Na}_2\text{O}$  in samples of basalt fragments from ocean floor dredges, calculated to 8 wt. %  $\text{MgO}$  to correct for low-pressure crystal fractionation (Klein and Langmuir, 1987). Sodium is incompatible in the crystal lattice of the mantle minerals olivine and orthopyroxene (Klein and Langmuir, 1987), which means

that it preferentially transitions out of solid mantle material and into a parcel of liquid melt. Sodium is therefore more highly concentrated in earlier melts, making  $\text{Na}_8$  a good indicator of the extent of partial melting. Low values of  $\text{Na}_8$  are expected in areas affected by a hotspot, where the mantle has undergone extensive melting. High values are often associated with long transform offsets, where cool temperatures result in lower degrees of melting.  $\text{Na}_8$  has been calculated for a number of ridges. For the Southeast Indian Ridge (SEIR), which spreads at an intermediate-rate,  $\text{Na}_8$  is in the range of 2.5 to 3.0 (Klein and Langmuir, 1987). The Galapagos Spreading Center has  $\text{Na}_8$  generally in the range of 2.0 to 2.3 (Klein and Langmuir, 1987). The slow-spreading MAR has  $\text{Na}_8$  in the range of 1.6 to 2.8, whereas  $\text{Na}_8$  for the fast-spreading EPR is in the range of 2.2 to 2.6 (Klein and Langmuir, 1987).

In this study,  $\text{Na}_8$  for ESR segments E2-E9 were calculated using data from Fretzdorff et al. (2002) and the method of Klein and Langmuir (1987). Additional values of  $\text{Na}_8$  for E1-E3 were obtained from Leat et al. (2000). A total of 81 samples with  $\text{Na}_8$  are available for the ESR (Fig. 11d). The segment with the greatest number is E2, for which there are 18 data points. However, only one value of  $\text{Na}_8$  is available for E1. To examine along-axis changes,  $\text{Na}_8$  was averaged for each segment (Fig. 11d). Along the length of the ESR,  $\text{Na}_8$  takes a roughly upside-down u-shaped trend. Segments E4 and E9 deviate from that trend, and the southern end of the ridge has slightly higher  $\text{Na}_8$ . The median of segment-averaged values of  $\text{Na}_8$  is 2.88, and the mean is 2.68. The lowest average values of  $\text{Na}_8$  are found at segments E1 and E4 (both 2.17), while the highest values occur at segments E5 and E6 (3.08 and 2.94, respectively).

Box plots were created to examine the  $\text{Na}_8$  data for outliers (Fig. 12). A sample was considered to be an outlier if it was above  $q_3 + 1.5(q_3 - q_1)$  or below  $q_1 - 1.5(q_3 - q_1)$ , where  $q_1$  and  $q_3$  are the 25<sup>th</sup> and 75<sup>th</sup> percentiles in the data, respectively. “Whiskers,” marked with dashed lines, denote the extent of the most extreme data points not considered outliers by the above criteria. Over the length of the ESR, no segments appear to be statistically anomalous in  $\text{Na}_8$ , based on the fact that no box

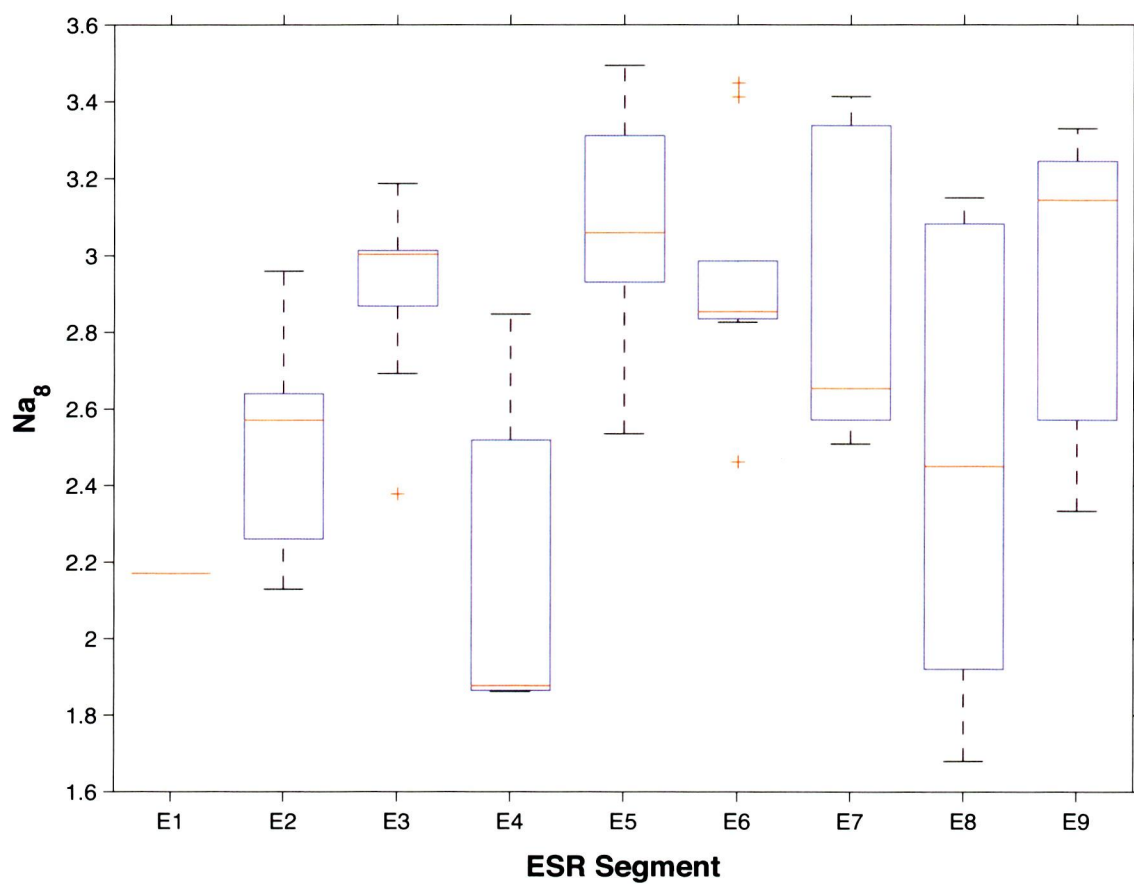


**Fig. 12.** Boxplots of  $Na_8$  for segments E1-E9. Blue boxes denote the 25<sup>th</sup> and 75<sup>th</sup> percentiles. Horizontal red lines show the median for each segment. Dashed lines denote “whiskers,” which extend to the farthest data points that are not considered outliers.



plot for any one segment fell out of the range of whiskers of all other segments. One sample for segment E3 and three samples for E6 were determined to be outliers. These samples were examined in detail, to determine if any geological or analytical reason supported elimination of their values in subsequent analyses. Two of the four samples were slightly vesicular pillow basalt with glassy rims, containing feldspar phenocrysts (Fretzdorff et al., 2002). The other two were slightly vesicular, glass-rimmed lavas (Fretzdorff et al., 2002). Thus, no obvious reason was found to eliminate these samples, and they were retained for all calculations and plots. As additional confirmation, a generalized extreme studentized deviate (ESD) test (Rosner, 1983) found no outliers for individual  $\text{Na}_8$  data points.

$\text{Fe}_8$  was calculated in the same manner as  $\text{Na}_8$ , using the concentration of FeO in rock samples taken from the seafloor corrected to 8 wt. % MgO (Klein and Langmuir, 1987). The concentration of FeO in a rock sample is related to the pressure at which it began melting, or the depth at which the adiabat crosses the solidus. Higher pressures of melting may be associated with anomalously hot mantle material, or a thick lithospheric lid that depresses the onset of melting to greater depths.  $\text{Fe}_8$  data are available to compare the ESR to other ridges. The SEIR has  $\text{Fe}_8$  in the range of 7.5 to 9.2 (Klein and Langmuir, 1987). For the Galapagos Spreading Center,  $\text{Fe}_8$  is roughly 9.2 to 9.9 (Klein and Langmuir, 1987). The MAR has  $\text{Fe}_8$  in the range of about 7.6 to 11.9, whereas  $\text{Fe}_8$  for the EPR is roughly 9.3 to 9.7 (Klein and Langmuir, 1987).

$\text{Fe}_8$  was calculated for data from Fretzdorff et al. (2002) and Leat et al. (2000) using the method of Klein and Langmuir (1987). Seventy-four values of  $\text{Fe}_8$  were obtained. The segment with the greatest number was E7, with 16 samples available (Fig. 11d). Segment averages of  $\text{Fe}_8$  form an upside-down u-shape, nearly identical to along-axis  $\text{Na}_8$ . Segments E4 and E9 deviate from this trend, similar to  $\text{Na}_8$ . Mean and median values of average  $\text{Fe}_8$  are 6.44 and 6.87, respectively. Box plots (Fig. 13) suggest that no individual samples are outliers for  $\text{Fe}_8$ , and no ESR segments are outliers for average  $\text{Fe}_8$ . However, an ESD test suggests that segments E1 and E4 are outliers for

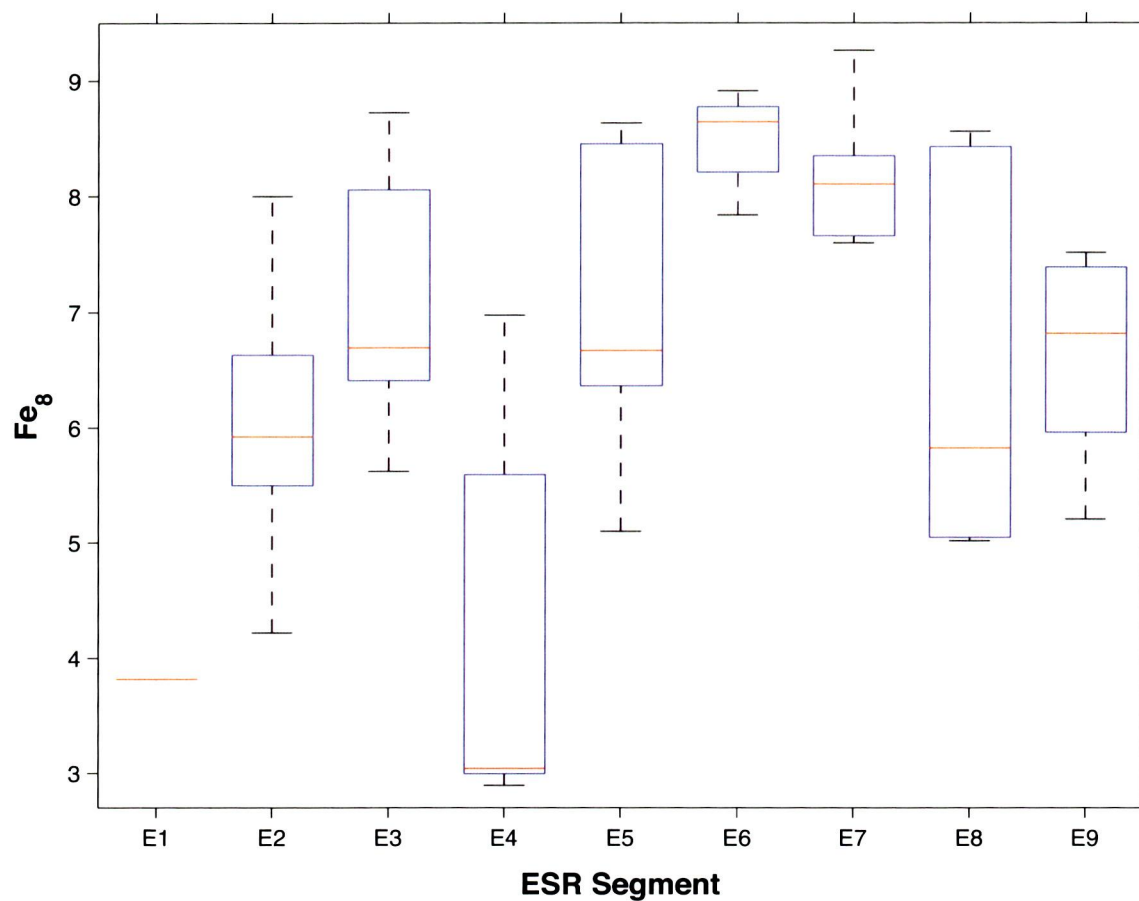


**Fig. 13.** Boxplots of  $Fe_8$  for segments E1-E9. Blue boxes denote the 25<sup>th</sup> and 75<sup>th</sup> percentiles. Horizontal red lines show the median for each segment. Dashed lines denote “whiskers,” which extend to the farthest data points that are not considered outliers.

average  $\text{Fe}_8$ . Only one sample is available for segment E1, and average  $\text{Fe}_8$  for segment E4 is 4.21.

*Isotopic source composition:  $^{87}\text{Sr}/^{86}\text{Sr}$*

The ratio of  $^{87}\text{Sr}$  to  $^{86}\text{Sr}$  is an indicator of mantle source composition at a MOR.  $^{87}\text{Sr}/^{86}\text{Sr}$  for normal MORB is about 0.7026 (Ito et al., 1987). Near hotspots,  $^{87}\text{Sr}/^{86}\text{Sr}$  ranges from about 0.7040 to 0.7050 (Ito et al., 2003).  $^{87}\text{Sr}/^{86}\text{Sr}$  ratios from Bouvet Island are about 0.7037 (le Roex et al., 1982; Kurz et al., 1998).  $^{87}\text{Sr}/^{86}\text{Sr}$  along the SWIR in the vicinity of the Bouvet plume generally range from 0.70267 to 0.70297 for normal MORB, from 0.70356 to 0.70364 for enriched basalts with plume characteristics, and from 0.70291 to 0.70370 for transitional basalts (le Roex et al., 1983).

$^{87}\text{Sr}/^{86}\text{Sr}$  values for segments E2-E9 were compiled from Fretzdorff et al. (2002) and Leat et al. (2000) (Fig. 11c). No published data are available for segment E1. Averages were calculated for segments E2-E9, yielding mean and median values of 0.7029 and 0.7028, respectively. The profile of  $^{87}\text{Sr}/^{86}\text{Sr}$  is roughly u-shaped (Fig. 11c). However, average  $^{87}\text{Sr}/^{86}\text{Sr}$  for segment E4 is much higher than most other segments, deviating from the u-shaped trend. The segments with the highest average  $^{87}\text{Sr}/^{86}\text{Sr}$  are E2, E4, and, to a lesser extent, E9. The segments with the lowest average  $^{87}\text{Sr}/^{86}\text{Sr}$  are E5, E6, and E7. Box plots were made for  $^{87}\text{Sr}/^{86}\text{Sr}$  in the manner described above for  $\text{Na}_8$  and  $\text{Fe}_8$  (Fig. 14). No samples were found to be outliers for  $^{87}\text{Sr}/^{86}\text{Sr}$ , and no ESR segments were determined to be outliers for average  $^{87}\text{Sr}/^{86}\text{Sr}$ .

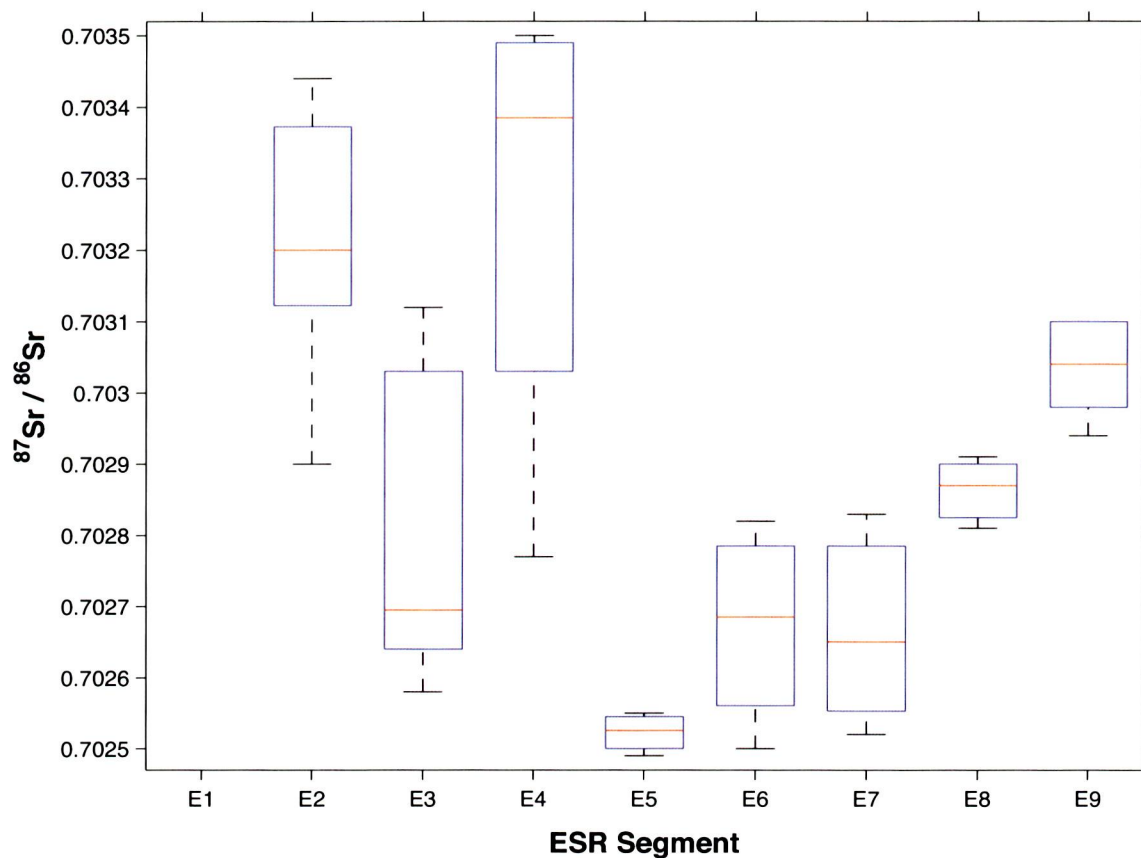


**Fig. 14.** Boxplots of  $^{87}\text{Sr}/^{86}\text{Sr}$  for segments E1-E9. Blue boxes denote the 25<sup>th</sup> and 75<sup>th</sup> percentiles. Horizontal red lines show the median for each segment. Dashed lines denote “whiskers,” which extend to the farthest data points that are not considered outliers.

## Regressions

As discussed in the Background chapter, previous studies (Lin et al., 1990; Cannat et al., 1999) have used plots of segment length vs.  $\Delta$ bathymetry to analyze the tectonic processes occurring at a ridge. Fig. 15 shows a comparison of segment length vs.  $\Delta$ bathymetry for the MAR, SWIR, and ESR. For each ridge regression lines have been fitted through the points for individual ridge segments. In general, regression line slopes are inversely proportional to the spreading rate of a ridge. The regression line for the SWIR, which is an ultra-slow spreading ridge, has the steepest slope (53.8 m/km). The slow-spreading MAR has a regression line with lower slope (16.1 m/km), and the ESR regression line is even shallower (3.51 m/km), as expected for an intermediate-rate ridge.

More broadly, beyond this relationship between segment length and  $\Delta$ bathymetry, a series of statistical regressions was used to explore the correlations between different types of geological data in the ESR region, with the goal of assessing the interrelationships between tectonic and magmatic processes in the area. Four variables were considered to be independent and six variables were treated as dependent, yielding a total of 24 regression calculations. Independent variables were segment length, segment spreading rate and two different determinations of ESR-SST separation distance. Segment length was calculated as the latitudinal distance separating the farthest north and farthest south points of a given ESR ridge segment. Spreading rates were obtained from Thomas et al. (2003), who used the width of the Brunhes anomaly from evenly spaced magnetic profiles to determine local relative plate motions for segments E2-E8. One method used to calculate ESR-SST separation distance was to find the shortest distance between each segment center and any point on the SST ( $\text{dist}_{\text{sst}}$ ). This distance was investigated because of its potential significance in the influence of subduction components on the ESR. The other method of determining separation distance calculated the distance from each segment center to the nearest subducting slab end ( $\text{dist}_{\text{slab\_end}}$ ). This distance provides a potential measure of

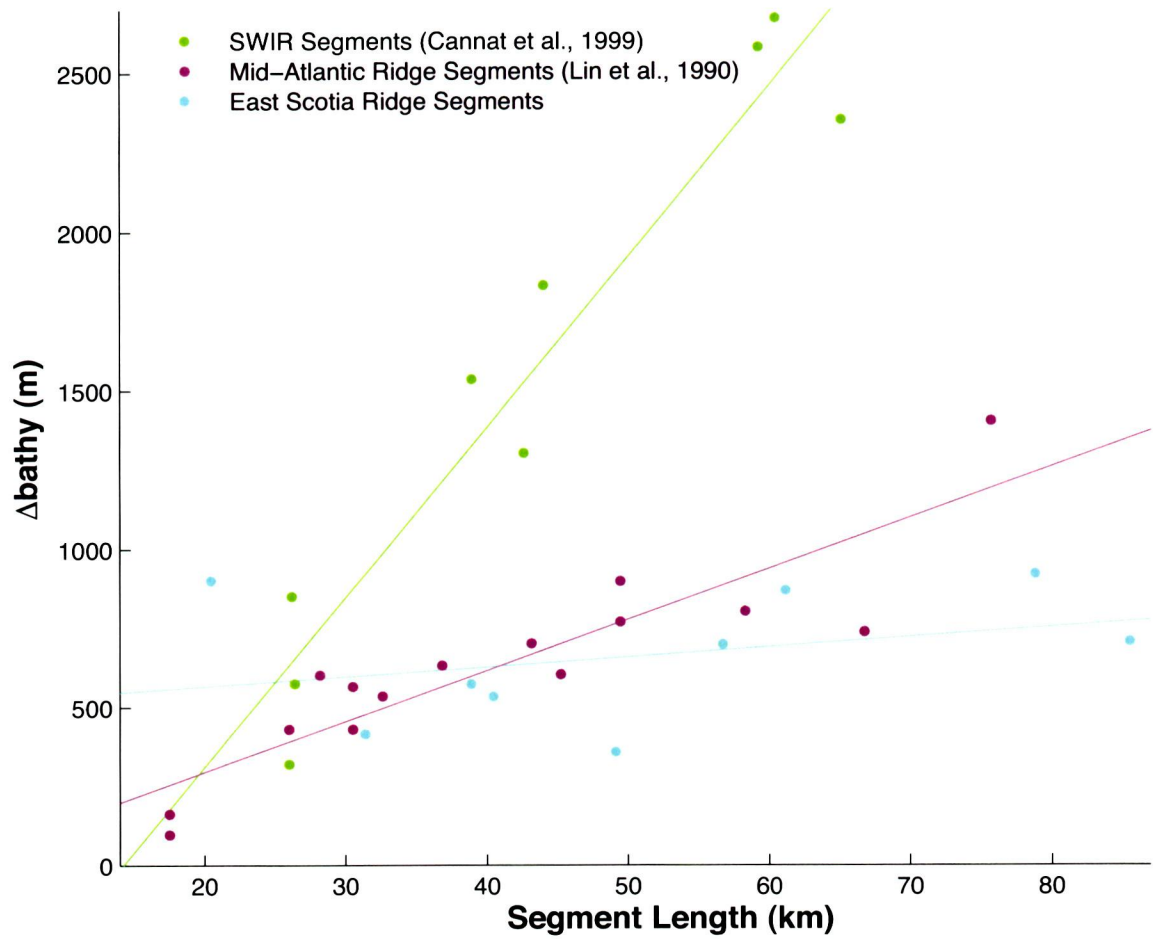


**Fig. 15.** Plots of segment length vs.  $\Delta$ bathymetry for the SWIR (Cannat et al., 1999), MAR (Cannat et al., 1999), and ESR.

mantle originating beneath SAM and flowing into the back-arc region. The six data types designated as dependent variables were  $\Delta\text{bathy}$ ,  $\Delta\text{MBA}$ ,  $\Delta\text{MBA}_{\text{det}}$ , segment-averaged  $\text{Na}_8$ , segment-averaged  $\text{Fe}_8$ , and segment-averaged  $^{87}\text{Sr}/^{86}\text{Sr}$ .

Many of the combinations of variables appeared to have little or no correlation with one another. Among all regressions, the highest r-squared was found for  $\text{dist}_{\text{sst}}$  and  $\text{Fe}_8$ , with a value of 0.568 (Fig. 16). A relatively high r-squared value, 0.489, was also calculated for  $\text{dist}_{\text{sst}}$  vs.  $^{87}\text{Sr}/^{86}\text{Sr}$ . For  $\text{dist}_{\text{slab\_end}}$ , the highest r-squared values are 0.559, 0.488, 0.488, and 0.364 for  $\text{Fe}_8$ ,  $^{87}\text{Sr}/^{86}\text{Sr}$ ,  $\Delta\text{MBA}$ , and  $\text{Na}_8$ , respectively. For segment length,  $\Delta\text{MBA}$  yielded the highest r-squared value: 0.280. The highest r-squared value for spreading rate was 0.298, which was for the  $\Delta\text{bathy}$  regression.

Low r-squared values among the regressions may in part be due to segment E4. There are several reasons suggesting that E4 is an anomalous segment. For example, the length of E4 is only slightly greater than that of E1, which is the shortest segment. Additionally, E4 is a propagating segment. Considering the short length of E4, much of the extent of the segment is affected by ridge propagation, suggesting that geological processes are not steady-state. Removing E4 from regression calculations results in much higher values of r-squared for  $\text{dist}_{\text{slab\_end}}$ : r-squared values for  $\text{Fe}_8$ ,  $^{87}\text{Sr}/^{86}\text{Sr}$ ,  $\text{Na}_8$ , and  $\Delta\text{bathy}$  become 0.911, 0.765, 0.625, and 0.485, respectively. Values of r-squared also increased for  $\text{dist}_{\text{sst}}$  upon removal of segment E4, to 0.888, 0.721, 0.611, and 0.409 for  $\text{Fe}_8$ ,  $\text{Na}_8$ ,  $^{87}\text{Sr}/^{86}\text{Sr}$ , and  $\Delta\text{bathy}$ , respectively. For the spreading rate regressions, all r-squared values increased with the removal of E4. The largest r-squared values for spreading rate were for  $^{87}\text{Sr}/^{86}\text{Sr}$ ,  $\Delta\text{bathy}$ , and  $\text{Fe}_8$ , at 0.422, 0.321, and 0.369, respectively. Upon removing segment E4 from regressions with segment length, r-squared increased for  $^{87}\text{Sr}/^{86}\text{Sr}$  from 0.013 to 0.317 and for  $\Delta\text{MBA}$  from 0.038 to 0.116. However, removing E4 resulted in decreases in r-squared for the other four parameters.

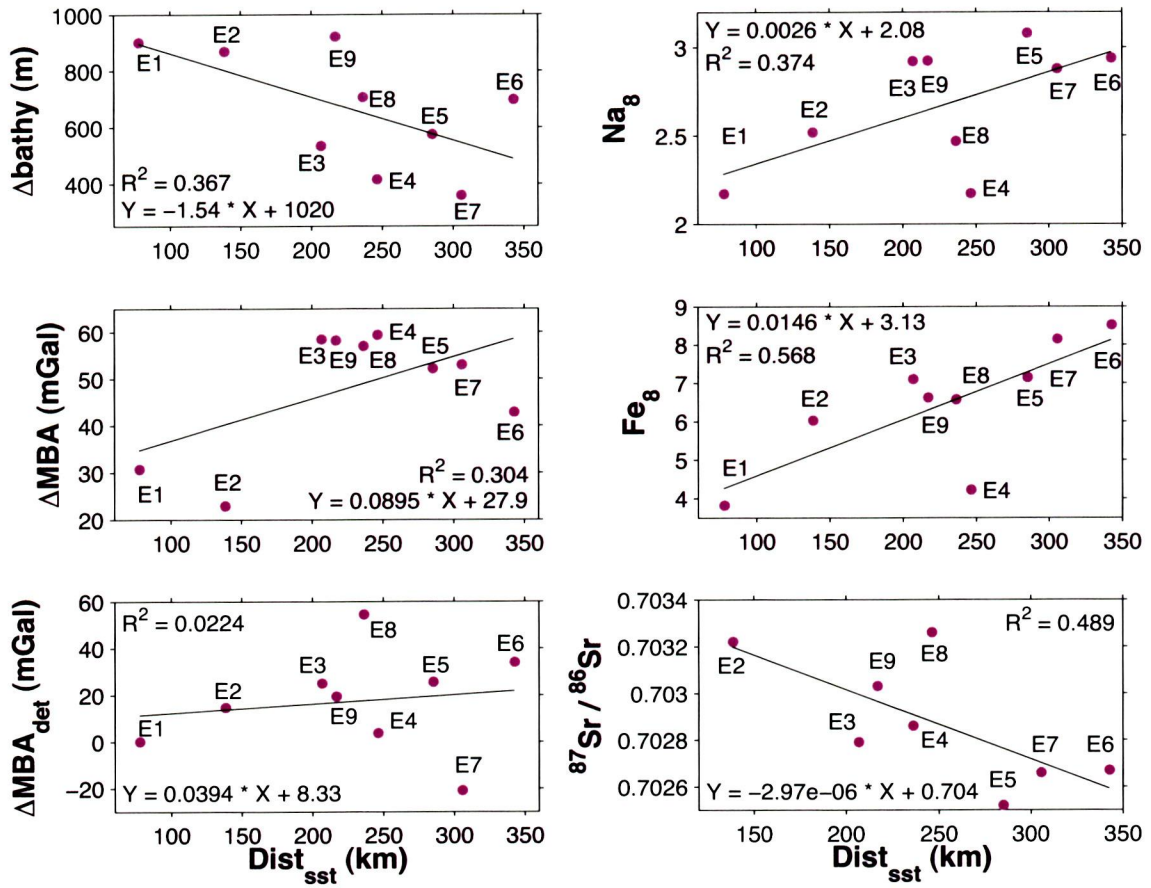


**Fig. 16.** Sample of six of a total of 24 regression plots. These plots treat  $\text{dist}_{\text{sst}}$  as the independent variable. Black lines are regression lines of best fit. Equations of regressions lines and r-squared values are included.



## DISCUSSION

### The Thermal Plume Mechanism as the Cause of Geophysical and Geochemical Variations in the ESR Region

Broadly speaking, either of two general hypotheses may explain the variation of bathymetry, MBA, or geochemistry in the Scotia region. One hypothesis invokes a “classic” thermal plume structure, with a connection in the upper mantle between the ESR and the location of the Bouvet conduit. An alternative hypothesis assumes that a large region of upper mantle in the southern Atlantic area, encompassing both the Scotia Sea and the Bouvet plume region, is heterogeneous in geochemical composition. Under this hypothesis, melting processes vary with plate boundary geometry, causing the expression of heterogeneities in bathymetry, gravity, and eruptive geochemistry to be related to the localized geological setting.

#### *Potential mechanism: Thermal plume hypothesis*

An end-member version of the plume-dominant hypothesis assumes that a “classic” thermal plume interacts in a steady-state fashion with the ESR, without involving mantle geochemical heterogeneity. In this model, a continuous flux of mantle material advects from the plume to the ESR. A variant of this model takes into account the westward displacement that the Scotia Arc has undergone relative to the African plate. Like the steady-state model, this plate-separation model assumes that a high flux of mantle material originates from a traditional, thermally buoyant plume. However, in the plate-separation model an initial connection could have been made between the Bouvet plume and the ESR long before a separation distance of 2,000 km would have become prohibitive for plume-ridge interactions. With an established connection between ridge and plume, the supply of mantle plume material to the ESR may have continued despite increasing separation distance. For example, the Réunion hotspot has interacted with the CIR for ~38 Ma, even as the separation

distance between the ridge and hotspot has grown to over 1,100 km (Morgan, 1978; Murton et al., 2005).

*Evaluation of the thermal plume hypothesis: Geophysical data*

Plume-influenced ridges are generally significantly shallower than “normal” spreading centers. For example, the MAR is above sea level where it crosses the ridge-centered Iceland hotspot (Ito et al., 2003). Likewise, the Galapagos Spreading Center becomes increasingly shallow over a distance longer than 1,000 km as it nears the Galapagos plume, reaching  $\sim 1.5$  km depth where the plume-ridge separation distance is a minimum,  $\sim 170$  km (Detrick et al., 2002; Chen and Lin, 2004). Although the centers of segments E2 and E9 are roughly 0.5 to 1.0 km shallower than those of other ESR segments, the depths of these segment centers are  $\sim 2.5$  km, which is approximately the same as average global mid-ocean ridge depth. If a plume affected E2 and E9, the overall depths of these two segments would be expected to be significantly shallower.

Along similar lines, when a plume affects part of a MOR, long-wavelength axial MBA low values are usually observed (e.g., Detrick et al., 2002; Ito et al., 2003). For example, an MBA profile along the MAR near the Iceland hotspot shows a u-shaped anomaly with an overall magnitude of approximately 270 mGal over a distance of  $\sim 2000$  km, with the lowest values of MBA centered on the postulated plume conduit (Ito and Lin, 1995; Ito et al., 2003). For the Galapagos/Galapagos Spreading Center system, the long-wavelength amplitude of MBA is about 90 mGal (Ito and Lin, 1995). For the ESR, however, MBA values do not show the general trends that are observed along most plume-affected ridges. Instead, higher values of MBA are found at the ESR segments with lower  $\text{dist}_{\text{sst}}$  and  $\text{dist}_{\text{slab-end}}$ , which presumably would be more affected by the inflow of Bouvet plume material at the slab ends.

*Evaluation of the thermal plume hypothesis: Geochemical data*

In general, average  $\text{Na}_8$  would be expected to be relatively lower along plume-affected portions of a ridge, where degree of melting is higher. Average  $\text{Na}_8$  for segment E2 is 2.52, which is significantly below the ESR mean of 2.68 with 89% confidence. However, averages of  $\text{Na}_8$  for segments E4 and E8 are lower than that of segment E2, and it is unlikely that plume flow influences those segments, at least to a greater degree than E2. Additionally, average  $\text{Na}_8$  is 2.93 for E9, which is above the ESR mean, suggesting that there is no plume affect on that segment. Thus,  $\text{Na}_8$  values for the ESR are not consistent with a simple model in which hot Bouvet plume material increases the degree of melting at the northernmost and southernmost segments of the ESR.

Similarly, if a plume affects the ESR by inflow at the slab ends, average  $\text{Fe}_8$  would be expected to be higher at segments E2 and E9 because of increased depth of melting. However, average  $\text{Fe}_8$  at segment E2 (6.02) is below both the ESR mean of 6.44 and the median of 6.87. Likewise, average  $\text{Fe}_8$  at segment E9 (6.62) is below the ESR median. While average  $\text{Fe}_8$  at E9 is greater than the ESR mean, there is only 61% confidence that average  $\text{Fe}_8$  data for E9 come from a sample with a mean greater than that of average ESR  $\text{Fe}_8$ . Thus,  $\text{Fe}_8$  data also do not unambiguously indicate plume influence on segments E2 and E9.

Globally, ridge segments that are affected by a plume normally show elevated levels of  $^{87}\text{Sr}/^{86}\text{Sr}$ , greater than 0.7030-0.7035 (Ito et al., 2003). However, average  $^{87}\text{Sr}/^{86}\text{Sr}$  ratios at segments E2 and E9 are 0.7032 and 0.7030, respectively. These values of  $^{87}\text{Sr}/^{86}\text{Sr}$  are more indicative of transitional, or T-type, basalts, which range from 0.70291 to 0.70370 along the SWIR (le Roex et al., 1983). Additionally, although T-type basalts may result from mixing of mantle with plume characteristics and typical depleted mantle, T-type lavas in the southern Atlantic along the AAR and SWIR have been also explained as the result of partial melting where veining comprises some of the source (le Roex et al., 1983).

*Evaluation of the thermal plume hypothesis: Geological data (ridge segmentation, propagation, and axial morphology)*

The nature of ridge axis morphology along the ESR does not clearly point to excess magmatism and plume influence. As noted earlier, axial valleys exist along almost the entire length of the ESR (Fig. 7). However, segments with axial highs are frequently observed along plume-influenced intermediate-rate ridges (Detrick et al., 2002). Thus, the presence of near-ubiquitous axial valleys along ESR segments also seems to contradict the hypothesis that the ESR is plume-affected.

As noted in the Results chapter, some ridge segments appear to be propagating toward the geographic center (near segment E6) of the ESR. Typically, ridge segments migrate away from plumes due to excess volcanism (e.g., Briaud and Rabinowicz, 2002). It is plausible that segments E2, E4, E5, and E9 are propagating due to an effect by the Bouvet plume. However, propagation may also occur because of a bathymetric gradient (e.g., Phipps Morgan and Parmentier, 1995) along the ESR.

Along sections of ridges that are not dominated by plume effects (i.e., tectonically-controlled ridges), plots of segment length vs.  $\Delta$ bathy generally show a positive, linear trend (Lin, 1990). Additionally, the slope of a fitted line is inversely proportional to the spreading rate (Lin, 1990). The relationship between segment length and  $\Delta$ bathy for the ESR follows the positive, linear trend established by the slow spreading MAR and ultra-slow spreading SWIR (Fig. 15), and the slope of the ESR regression is lower than the MAR and SWIR. This implies that segment-scale tectonics are an important control on individual ESR segment centers.

**Alternative Mechanism: Mantle Geochemical Heterogeneity**

A geochemically-based alternative to the purely thermal plume hypothesis does not require continuous advection of material between the Bouvet plume and the ESR, and in fact might not require the existence of a plume whatsoever (Fig. 17). The geo-

chemical and geophysical characteristics of the ESR could be explained by a “plum-pudding” model (le Roex et al., 1983; le Roex et al., 1985; Standish et al., 2008) in which the mantle source material that enters the melting region of the ESR has a heterogeneous geochemical composition (Fig. 17). In the “plum-pudding” model, eclogite or pyroxenite veins are distributed throughout a peridotite matrix. The fertile material from these veins can begin melting at depths greater than the solidus of the surrounding peridotite (Anderson, 2004; Korenaga, 2005). Thus, a veined mantle may melt more than a geochemical homogeneous mantle even without a temperature anomaly.

This geochemical hypothesis postulates that enhanced melting of a heterogeneous mantle is modulated by plate boundary geometry. For example, such an effect might explain the broad region of elevated seafloor and other anomalies observed around the Bouvet Triple Junction. As discussed in the Background chapter, gravity and bathymetry data suggest that the Bouvet plume influence is relatively localized, to a distance of only approximately 300 km along the SWIR (Georgen et al., 2001). Additionally,  $^3\text{He}/^4\text{He}$  data suggest that the Bouvet plume’s influence along the SWIR extends less than 500 km to the east (Georgen et al., 2003), and that  $^3\text{He}/^4\text{He}$  may not be elevated to the west along the AAR (Kurz et al., 1998). Previous studies have shown that elevated  $^3\text{He}/^4\text{He}$  ratios may be associated with the central core of a plume (e.g., Kurz and Geist, 1999), and therefore may serve as an indicator of the region most influenced by the plume conduit. Other types of geochemical data, such as  $^{143}\text{Nd}/^{144}\text{Nd}$ ,  $\text{Zr}/\text{Nb}$ ,  $\text{Y}/\text{Nb}$ ,  $\text{Zr}/\text{Y}$ ,  $\text{La}/\text{Yb}_\text{N}$ , and  $(\text{La}/\text{Sm})_\text{N}$  (le Roex et al., 1983; le Roex et al., 1985), indicate a much broader distribution of basalts with characteristics similar to transitional MORB and enriched MORB, with anomalies over 700 km to the east of Bouvet Island (le Roex et al., 1983; le Roex et al., 1985) and ~1,200 km to the west, via the AAR (le Roex et al., 1983; le Roex et al., 1985).

It is possible that the broad geochemical anomalies observed in the vicinity of the Bouvet Triple Junction may not be entirely due to the Bouvet plume. Numerical

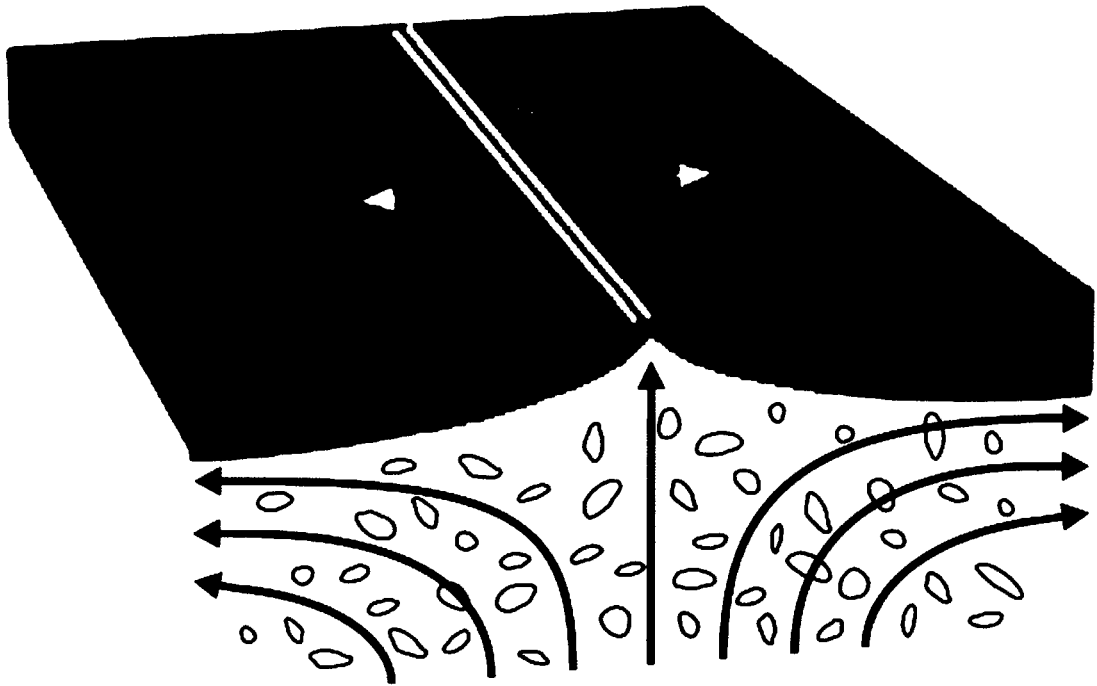


**Fig. 17.** Schematic of a heterogeneous mantle beneath a MOR. Lines and arrows in the mantle show the direction of upwelling beneath a ridge. Irregularly shaped geochemical heterogeneities are shown throughout the mantle.

models have suggested that mantle upwelling at plate boundary triple junctions may be different from that at a single ridge (Georgen and Lin 2002; Georgen, 2008; Georgen and Sankar, 2010). Because of the juxtaposition of the upwelling fields of three ridge axes at a triple junction, mantle temperatures and crustal production might be higher than in a single-ridge setting. For example, in a model that does not incorporate a thermal plume or geochemical heterogeneity, crustal thickness is predicted to increase approximately 6 km within 200 km of a triple junction such as Azores Triple Junction or BTJ (Georgen, 2008). The addition of source heterogeneity into such a model is likely to increase the amplitude and spatial distribution of anomalies in seafloor depth, gravity, and basalt geochemistry.

In the case of the ESR, a back-arc ridge intersects a subduction trench. A seismic anisotropy study of the Scotia region revealed fast flow directions parallel to the ridge axis in the northern portion of the ESR, consistent with inflow occurring through a slab tear zone (Müller et al., 2008). Although similar seismic anisotropy results do not exist in the southern portion of the ridge due to a lack of data coverage, northward-directed flow through the southern slab tear would be consistent with geodynamic processes observed in similar subduction settings, such as the Tonga Trench (Keller et al., 2008). Thus, it is possible that mantle from beneath SAM and ANT enters the ESR region. In that case, the superposition of ridge-parallel mantle flow and corner flow associated with plate separation could increase the flux through the melt triangle, thereby enhancing the magma budget of the northernmost and southernmost segments of the ESR. The existence of a veined mantle source within the Scotia area could result in even more enhanced melting in the northern and southern portions of the ESR, thereby increasing the differences between the central and distal segments of the ridge.

It is important to note that, while geochemical heterogeneities can enhance melting beneath a spreading ridge, such a mechanism is not required to act in isolation. For example, it is possible for geochemical heterogeneities to amplify the effects of a

thermal anomaly (Fig. 18). If a geochemically heterogeneous mantle is present, a small thermal anomaly may be sufficient to produce a large melting effect.

In summary, direct flow of Bouvet plume mantle into ESR seems unlikely, even allowing for plume-ridge interaction extended by plate separation. Instead, a role of geochemical heterogeneity in the mantle is favored, particularly since this explanation has been invoked for other regions in the south Atlantic with complex plate geometry. The existence of a small thermal heterogeneity cannot be ruled out from MBA, but if it exists, it must be considerably smaller in magnitude than, for example, those in the Iceland or Galapagos systems.



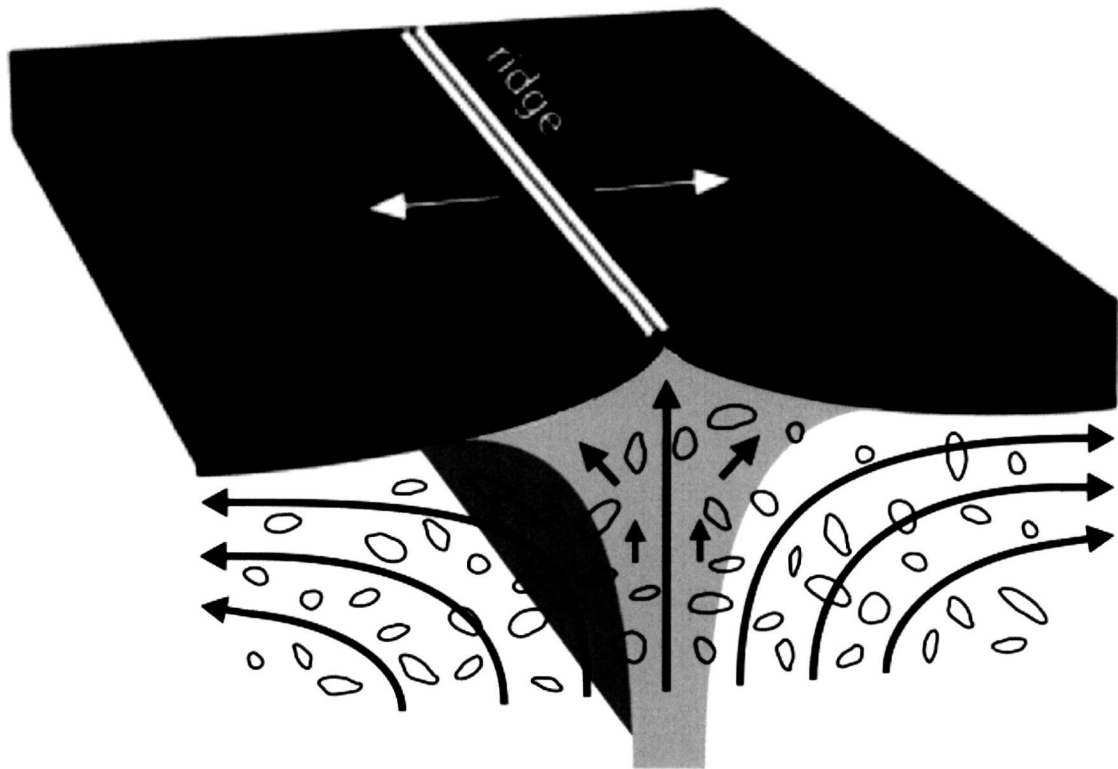


**Fig. 18.** Schematic of a geochemically heterogeneous mantle with plume. Curved lines, which spread out horizontally in the mantle, show the direction of upwelling beneath a ridge. Irregularly shaped geochemical heterogeneities are shown throughout the mantle. Dark grey indicates spreading lithospheric plates and the grey regions beneath the ridge represent a plume.

## CONCLUSIONS

The main results of this study of geological processes along the ESR include the following:

- (1) Geophysical data (e.g., bathymetry and MBA) along the ESR do not have the characteristics of a “classic” plume-affected ridge like the Galapagos Spreading Center. This is also the case for geochemical data. For example,  $^{87}\text{Sr}/^{86}\text{Sr}$  is not elevated to levels consistent with a mantle plume. Additionally, geologic data show a presence of axial valleys, which is not typical for ridge segments affected by a mantle plume. Plots of segment length vs.  $\Delta\text{bathy}$  are consistent with ridges that are unaffected by a plume. Overall, geophysical data provide evidence against the hypothesis, suggested by earlier studies (e.g., Livermore, 2003), that direct flow from the Bouvet plume affects ESR segments.
- (2) The geophysical, geochemical, and geological variability along the ESR may be explained by complex plate boundary geometry and geochemical heterogeneity in the mantle source. This explanation is consistent with geochemical heterogeneity inferred for adjacent areas in the southern Atlantic Ocean by earlier studies (le Roex et al., 1983; le Roex et al., 1985; le Roex et al., 1992; Standish et al., 2008). Under this mechanism, mantle flowing into the ESR subridge region would add to the corner flow due to plate separation, causing the flux of more material through the melting region. The presence of geochemical heterogeneities in the mantle source region could additionally increase the production of melt.

## REFERENCES

- Anderson, M.L., Zandt, G., Triep, E., Fouch, M., Beck, S., 2004. Anisotropy and mantle flow in the Chile-Argentina subduction zone from shear wave splitting analysis. *Geophys. Res. Lett.* 31, L23608, doi:10.1029/2004GL020906.
- Blakely, R.J., 1996. *Potential Theory in Gravity & Magnetic Applications*. Cambridge University Press, p. 441.
- Briaies, A., Rabinowicz, M., 2002. Temporal variations of the segmentation of slow to intermediate spreading mid-ocean ridges 1. Synoptic observations based on satellite altimetry data. *J. Geophys. Res.* 107 (B5), 2098.
- Canales, J.P., Ito, G., Detrick, R.S., Sinton, J., 2002. Crustal thickness along the western Galápagos Spreading Center and the compensation of the Galápagos hotspot swell. *Earth Planet. Sci. Lett.* 203, 311-327.
- Cannat, M., Rommevaux-Jestin, C., Sauter, D., Deplus, C., Mendel, V., 1999. Formation of the axial relief at the very slow spreading Southwest Indian Ridge (49° to 69°E). *J. Geophys. Res.* 104 (B10), 22,825-22,843.
- Carbotte, S.M., Macdonald, K.C., 1994. The axial topographic high at intermediate and fast spreading ridges. *Earth Planet. Sci. Lett.* 128, 85-97.
- Chen, Y.J., Lin, J., 2004. Sensitivity of ocean ridge thermal structure to changes in magma supply: the Galápagos Spreading Center. *Earth Planet. Sci. Lett.* 221, 263-273.
- Cunningham, W.D., Dalziel, I.W.D., Lee, T.Y., Lawver, L.A., 1995. Southernmost South America-Antarctic Peninsula relative plate motions since 84 Ma: implications for the tectonic evolution of the Scotia Arc region. *J. Geophys. Res.* 100 (B5), 8257-8266.
- Detrick, R.S., Sinton, J.M., Ito, G., Canales, J.P., Behn, M., Blacic, T., Cushman, B., Dixon, J.E., Graham, D.W., Mahoney, J.J., 2002. Correlated geophysical, geochemical, and volcanological manifestations of plume-ridge interaction along the Galápagos Spreading Center. *Geochem. Geophys. Geosyst.* 3, 8501, doi:10.1029/2002GC000350.

- Divins, D.L., 2009. NGDC total sediment thickness of the world's oceans and marginal seas. <http://www.ngdc.noaa.gov/mgg/sedthick/sedthick.html>.
- Eagles, G., Livermore, R.A., Fairhead, J.D., Morris, P., 2005. Tectonic evolution of the west Scotia Sea, *J. Geophys. Res.* 110, 2401.
- Fretzdorff, S., Livermore, R.A., Devey, C.W, Leat, P.T., Stoffers P., 2002. Petrogenesis of the back-arc East Scotia Ridge, South Atlantic Ocean. *J. Petrol.* 43, 1435–1467.
- Georgen, J.E., 2008. Mantle flow and melting beneath oceanic ridge-ridge-ridge triple junctions. *Earth Planet. Sci. Lett.* 270, 231-240.
- Georgen, J.E., Kurz, M.D., Dick, H.J.B., Lin, J., 2003. Low  $^3\text{He}/^4\text{He}$  ratios in basalt glasses from the western Southwest Indian Ridge ( $10^\circ$ - $24^\circ\text{E}$ ). *Earth Planet. Sci. Lett.* 206, 509-528.
- Georgen, J.E., Lin, J., 2002. Three-dimensional passive flow and temperature beneath ocean ridge-ridge-ridge triple junctions. *Earth Planet. Sci. Lett.* 204, 115-132.
- Georgen, J.E., Lin, J., Dick, H.J.B., 2001. Evidence from gravity anomalies for interactions of the Marion and Bouvet hotspots with the Southwest Indian Ridge: effects of transform offsets. *Earth Planet. Sci. Lett.* 187, 183-300.
- Georgen, J.E., Sankar, R.D., 2010. Effects of ridge geometry on mantle dynamics in an oceanic triple junction region: implications for the Azores Plateau. *Earth Planet. Sci. Lett.* 298, 23-34.
- Ito, G., Lin, J., 1995. Oceanic spreading center-hotspot interactions: constraints from along-isochron bathymetric and gravity anomalies. *Geology* 23, 657-660.
- Ito, G., Lin, J., Graham, D., 2003. Observational and theoretical studies of the dynamics of mantle plume-mid-ocean ridge interaction. *Rev. Geophys.* 41 (4), 1017.
- Ito E., White W.M., Göpel C., 1987. The oxygen, strontium, neodymium, and lead isotope geochemistry of MORB. *Chem. Geol.* 62, 157–176.
- Keller, N.S., Arculus, R.J., Hermann, J., Richards, S., 2008. Submarine back-arc lava with arc signature: Fonualei Spreading Center, northeast Lau Basin, Tonga. *J. Geophys. Res.* 113.
- Klein, E.M., Langmuir, C.H., 1987. Global correlations of ocean ridge basalt chemistry with axial depth and crustal thickness. *J. Geophys. Res.* 92, 8089-8115.

- Korenaga, J., 2005. Why did not the Ontong Java Plateau form subaerially? *Earth Planet. Sci. Lett.* 234, 385–399.
- Kuo, B.Y., Forsyth, D.W., 1988. Gravity anomalies of the ridge-transform system in the South Atlantic between 31° and 34.5°S: upwelling centers and variation in crustal thickness. *Geophys. Res.* 10, 205–232.
- Kurz, M.D., le Roex, A.P., Dick, H.J.B., 1998. Isotope geochemistry of the oceanic mantle near the Bouvet triple junction, *Geochim. Cosmochim. Acta* 62, 841–852.
- Kurz, M.D., Geist, D., 1999. Dynamics of the Galápagos hotspot from helium isotope geochemistry, *Geochim. Cosmochim. Acta*, 63, 4139–4156.
- Lagabrielle, Y., Godd  ris, Y., Donnadi  u, Y., Malavieille, J., Suarez, M., 2009. The tectonic history of Drake Passage and its possible impacts on global climate. *Earth Planet. Sci. Lett.* 279, 197–211.
- le Roex, A.P., Dick, H.J.B., Erlank, A.J., Reid, A.M., Frey, F.A., Hart, S.R., 1983. Geochemistry, mineralogy and petrogenesis of lavas erupted along the Southwest Indian Ridge between the Bouvet Triple Junction and 11 degrees east. *J. Petrol.* 24, 267–318.
- le Roex A.P., Dick H.J., Reid A.M., Erlank A.J., 1982. Ferrobasalts from the Speiss Ridge segment of the Southwest Indian Ridge. *Earth Planet. Sci. Lett.* 60, 437–451.
- le Roex A.P., Dick H.J., Reid A.M., Frey, F.A., Erlank A.J., Hart, S.R., 1985. Petrology and geochemistry of basalts from the American-Antarctic Ridge, Southern Ocean: implications for the westward influence of the Bouvet mantle plume, *Contrib. Mineral. Petrol.* 90, 367–380.
- le Roex, A.P., Dick, H.J.B., Watkins, R.T., 1992. Petrogenesis of anomalous K-enriched MORB from the Southwest Indian Ridge: 11°53'E to 14°38'E, *Contrib. Mineral. Petrol.* 110, 253–268.
- Leat, P.T., Livermore, R.A., Millar, I.L., Pearce, J.A., 2000. Magma supply in back-arc spreading centre segment E2, East Scotia Ridge. *J. Petrol.* 41, 845–866.
- Lin, J., Phipps Morgan, J., 1992. The spreading rate dependence of three-dimensional mid-ocean ridge gravity structure, *Geophys. Res. Lett.* 19 (1), 13–16.

- Lin, J., Purdy, G.M., Schouten, H., Sempere, J.C., Zervas, C., 1990. Evidence from gravity data for focused magmatic accretion along the Mid-Atlantic Ridge. *Nature* 344 (6267), 627-632.
- Livermore, R., 2003. Back-arc spreading and mantle flow in the East Scotia Sea. From: Larter, R.D., Leat, P.T., 2003. Intra-Oceanic Subduction Systems: tectonic and magmatic Processes. Geologic Society of London, Special Publications 219, 315-331.
- Macdonald, K.C., Fox, P.J., Perram, L.J., Eisen, M.F., Miller, S.P., Carbotte, S.M., Cormier, M.-H., Shor, A.N., 1988. A new view of the mid-ocean ridge from the behaviour of ridge-axis discontinuities. *Nature* 335, 217-225.
- Moreira, M., All gre, C., 2002. Rare gas systematics on Mid-Atlantic Ridge (37–40 N), *Earth Planet. Sci. Lett.* 198, 401–416.
- Moreira, M., Doucelance, R., Kurz, M.D., Dupr , B., All gre, C., 1999. Helium and lead isotope geochemistry of the Azores Archipelago, *Earth Planet. Sci. Lett.* 169, 489–205.
- Morgan, W.J., 1978. Rodriguez, Darwin, Amsterdam, . . . , A second type of hotspot island, *J. Geophys. Res.* 83 (B11), 5355–5360.
- M ller, C., Bayer, B., Eckstaller, A., Miller, H., 2008. Mantle flow in the South Sandwich subduction environment from source-side shear wave splitting. *Geophys. Res. Lett.* 35, doi:10.1029/2007GL032411.
- Murton, B.J., Tindle, A.G., Milton, A.G., Sauter, D., 2005. Heterogeneity in southern Central Indian Ridge MORB: implications for ridge-hot spot interaction. *Geochem., Geophys., Geosyst.* 6 (3), doi:10.1029/2004GC000798.
- Parker, R.L., 1973. The rapid calculation of potential anomalies, *Geophys. J. R. Astron. Soc.* 31, 447-455.
- Parsons B., Sclater J.G., 1977. An analysis of the variation of ocean floor bathymetry and heat flow with age. *J. Geophys. Res.* 82, 803-827.
- Pearce, D.W., Leat, P.T., Barker, P.F., Millar, I.L., 2001. Geochemical tracing of Pacific-to-Atlantic upper mantle flow through the Drake Passage. *Nature* 410, 457–461.

- Phipps Morgan, J., Parmentier, E.M., 1995. Crenulated seafloor: evidence for spreading-rate dependent structure of mantle upwelling and melting beneath a mid-oceanic spreading center. *Earth Planet. Sci. Lett.* 129, 73–84.
- Ribe, N.M., 1996. The dynamics of plume-ridge interaction 2. Off-ridge plumes, *J. Geophys. Res.* 101 (B7), 16,195-16,204.
- Rosner, B., 1983. Percentage points for a generalized ESD many-outlier procedure. *Technometrics* 25 (2), 165-172.
- Sandwell, D.T., Smith, W.H.F., 2009. Global marine gravity from retracked Geosat and ERS-1 altimetry: ridge segmentation versus spreading rate. *J. Geophys. Res.* 114, doi:10.1029/2008JB006008.
- Schreider, A.A., Schreider, A.I., Kashintsev, G.L., Galindado-Zaldivar, J., Maldonado, A., Boiko, A.N., Evsenko, E.I., 2011. Peculiarities of the East Scotia ridge's geochronology. *Marine Geology* 51 (6), 1047-1060.
- Smith, W.H.F., Sandwell, D.T., 1997. Global seafloor topography from satellite altimetry and ship depth soundings. *Science* 277, 1957-1962.
- Standish, J.J., Dick, H.J.B., Michael, P.J., Melson, W.G., O'Hearn, T., 2008. MORB generation beneath the ultraslow spreading Southwest Indian Ridge (9°-25°E): major element chemistry and the importance of process versus source. *Geochem. Geophys. Geosyst.* 9 (5), doi:10.1029/2008GC001959.
- Thomas, C., Livermore, R., Pollitz, F., 2003. Motion of the Scotia Sea plates, *Geophysical Journal International* 155 (441), 789-804.
- Toomey, D.R., Hooft, E.E.E., Solomon, S.C., James, D.E., Hall, M.L., 2001. Upper mantle structure beneath the Galápagos Archipelago from body wave data, *Eos Trans. AGU*, 82 (47), Fall Meet. Suppl., Abstract T41D-04.

## **VITA**

**Briton Lee Nicholson**

**Old Dominion University  
Department of Ocean, Earth, and Atmospheric Sciences  
4600 Elkhorn Avenue, Room 406  
Norfolk, Virginia 23529  
bnich008@odu.edu  
757-819-8034**

### **Education**

**Naval Nuclear Power School, 2000  
Naval Nuclear Power Prototype, 2000  
A.S. Tidewater Community College, 2006  
B.S. Applied Mathematics/Geology, Old Dominion University, 2009**

### **Scholarships**

**Virginian Pilot Scholarship, 2008**

### **Awards and Honors**

**President's Honor Roll at Tidewater Community College, 2005-2007  
Magna Cum Laude graduation from Tidewater Community College, 2006  
Dean's List at Old Dominion University, 2008  
Magna Cum Laude graduation from Old Dominion University, 2009**

### **Skills and Qualifications**

**Experience with Unix, Fortran, Generic Mapping Tools, and Simulink  
Earned "A" letter grade in C++ programming course  
Highly proficient in Matlab programming  
Completed ESRI training for "Learning ArcGIS Desktop" and "Learning ArcGIS  
Spatial Analyst"  
Microsoft Excel, Access, and PowerPoint**

### **Research**

**Gravity anomalies of the seafloor along the East Scotia Ridge  
Magmatic and tectonic controls on crustal accretion  
Acceptance to Fall, 2010 American Geophysical Union conference**